

**THÈSE DE DOCTORAT
DE SORBONNE UNIVERSITÉ**

Spécialité : Physique

École doctorale n°564: Physique en Île-de-France

réalisée

au Laboratoire Kastler Brossel

sous la direction de Pierre-François Cohadon

présentée par

Pierre-Edouard Jacquet

pour obtenir le grade de :

DOCTEUR DE SORBONNE UNIVERSITÉ

Sujet de la thèse :

Progress towards cryogenic squeezed light optomechanics

soutenue le ????? 2025

devant le jury composé de :

M.	Mr.	Rapporteur
M.	Mr.	Rapporteur
M.	Mr.	Examinateur
Mme.	coucou	Examinateuse
Mme.	salut	Présidente du Jury
M.	aurevoir	Directeur de thèse



Remerciements

Merci bien

Contents

I Introduction	3
I.1 Historical background	3
I.2 State of the art	3
I.3 Relevance of this work	3
II Theory: Background	5
II.1 Quantum Optics	6
II.1.1 Quantum Description of Light	6
II.1.2 Coherent and Squeezed States	9
II.1.3 Sidebands and Quantum Noises	14
II.1.4 Quantum Sideband Diagram	19
II.2 Optical Cavities: Basics	19
II.2.1 Cavity types and Resonance Conditions	19
II.2.2 Spatial and Longitudinal Modes	19
II.2.3 Quantum Langevin Equations	19
II.3 Numerical Methods and Simulations	22
III Theory: Frequency Dependent Squeezing & Membrane based Optomechanics	23

III.1 Frequency Dependent Squeezing	24
III.2 Cavity Optomechanics with Membrane based systems	24
III.2.1 Radiation Pressure Coupling	24
III.2.2 Quantum Langevin Equations	24
III.2.3 Mechanical Resonators	24
III.2.4 Noise spectra	24
IV Experimental Methods	27
IV.1 Optical Locking Techniques with PyRPL	28
IV.1.1 Proportion-Integral (PI) Controllers	28
IV.1.2 Temperature Locks	30
IV.1.3 Optical paths Locks - Dither Locks	30
IV.1.4 Side of Fringe Locks	31
IV.1.5 Pound-Drever-Hall Locks	31
IV.1.6 Offset frequency Locks	32
IV.1.7 Coherent Sideband Locks	32
IV.1.8 PyRPL Control Implementation	32
IV.2 Optical Cavities and Squeezed Light Generation	32
IV.2.1 Cavity Types and Alignment Procedures	33
IV.2.2 Bowtie-type Optical Parametric Oscillator (OPO)	33
IV.2.3 Phase Matching and Nonlinear Crystals	33
IV.2.4 Filter Cavities for Squeezing Rotation	33
IV.3 Quadrature Measurement Techniques	33
IV.3.1 Direct Detection with Photodiodes	33
IV.3.2 Balanced Homodyne Detection	33
IV.3.3 Local Oscillator Design and Control	33

V Experiments: Optomechanics	35
V.1 System Description and Setup	36
V.1.1 Previous LKB work and Motivation	36
V.1.2 Specifications and Design	37
V.1.3 Flexure Actuation	42
V.1.4 Experimental Setup	43
V.1.5 Alignment Procedures	45
V.2 Experimental Characterization	47
V.2.1 Cavity Scans and Resonance Fitting	47
V.2.2 Locking Techniques and Stability	47
V.2.3 Optical Ringdowns and Loss Measurements	47
V.2.4 Mechanical Resonator Characterization	47
V.2.5 Bistability	47
V.3 Design of an Optomechanical Fibered Cavity	47
V.3.1 Design considerations	47
VI Experiments: Squeezed Light	49
VI.1 OPO Resonance and Locking	50
VI.1.1 Resonance Conditions and Sweeps	50
VI.1.2 Lock Acquisition and Optimization	50
VI.1.3 Stability Characterization	50
VI.2 Quadrature Spectral Analysis	50
VI.2.1 Detection of Squeezing and Anti-squeezing	50
VI.2.2 Spectral Variation with Frequency	50
VI.2.3 Optimal Quadrature Conditions	50
VI.3 Filter Cavity Concept	50

VI.3.1 Virgo Filter Cavity	50
VI.3.2 Thermal effects in bichromatic locks	50
Appendix: PDH Derivation	53
Appendix: Spectra Derivation	57

Chapter I

Introduction

Contents

I.1	Historical background	3
I.2	State of the art	3
I.3	Relevance of this work	3

I.1 Historical background

I.2 State of the art

I.3 Relevance of this work

Chapter II

Theory: Background

This chapter will cover the elementary concepts required to describe an membrane based optomechanical system in a quantum regime. We will first recall basics on optical field quantization as well describing coherent and squeezed light field, to then turn to the more specific frequency dependent squeezed light field. Secondly, we will cover the mathematical description of a mechanical resonator interacting with a generic coherent optical field, highlighting the differences with the seminal optomechanical system of a mirror on a spring. Finally, we will derive the equations of motions of a membrane based optomechanical system with frequency dependent squeezed optical fields.

Contents

II.1 Quantum Optics	6
II.1.1 Quantum Description of Light	6
II.1.2 Coherent and Squeezed States	9
II.1.3 Sidebands and Quantum Noises	14
II.1.4 Quantum Sideband Diagram	19
II.2 Optical Cavities: Basics	19
II.2.1 Cavity types and Resonance Conditions	19
II.2.2 Spatial and Longitudinal Modes	19
II.2.3 Quantum Langevin Equations	19
II.3 Numerical Methods and Simulations	22

II.1 Quantum Optics

II.1.1 Quantum Description of Light

Quantised Electromagnetic Field

We consider the quantised electromagnetic field in a volume V . The electric field operator can be written as

$$\hat{\mathbf{E}}(\mathbf{r}, t) = i \sum_{\ell} \mathcal{E}_{\ell} \left[\hat{a}_{\ell} \mathbf{f}_{\ell}(\mathbf{r}) e^{-i\omega_{\ell}t} - \hat{a}_{\ell}^{\dagger} \mathbf{f}_{\ell}^*(\mathbf{r}) e^{+i\omega_{\ell}t} \right], \quad (\text{II.1})$$

where $\mathcal{E}_{\ell} = \sqrt{\frac{\hbar\omega_{\ell}}{2\varepsilon_0 V}}$ is the field amplitude per photon in mode ℓ , \hbar is the reduced Planck constant, ω_{ℓ} is the angular frequency of mode ℓ , and ε_0 is the vacuum permittivity. The spatial mode functions $\mathbf{f}_{\ell}(\mathbf{r})$ form an orthonormal basis in V according to

$$\int_V d^3r \mathbf{f}_{\ell}^*(\mathbf{r}) \cdot \mathbf{f}_{\ell'}(\mathbf{r}) = \delta_{\ell\ell'}.$$

The annihilation and creation operators $\hat{a}_{\ell}(t)$ and $\hat{a}_{\ell}(t)^{\dagger}$ satisfy the canonical commutation relations

$$[\hat{a}_{\ell}, \hat{a}_{\ell'}^{\dagger}] = \delta_{\ell\ell'}, \quad [\hat{a}_{\ell}, \hat{a}_{\ell'}] = 0, \quad [\hat{a}_{\ell}^{\dagger}, \hat{a}_{\ell'}^{\dagger}] = 0$$

The explicit time dependence of the operators allows one to describe both slow classical modulations of the field and the intrinsic quantum fluctuations.

Fock basis

In this description of the optical field, each mode ℓ is modeled as a quantum harmonic oscillator with a discrete set of energy eigenstates known as *Fock states* or number states, denoted $|n_{\ell}\rangle$. These states form an orthonormal basis and satisfy $\hat{n}_{\ell}|n_{\ell}\rangle = n_{\ell}|n_{\ell}\rangle$, where \hat{n}_{ℓ} is the number operator defined by

$$\hat{n}_{\ell} = \hat{a}_{\ell}^{\dagger} \hat{a}_{\ell}.$$

The action of the creation and annihilation operators on these states is given by

$$\hat{a}_{\ell}|n_{\ell}\rangle = \sqrt{n_{\ell}}|n_{\ell}-1\rangle, \quad \hat{a}_{\ell}^{\dagger}|n_{\ell}\rangle = \sqrt{n_{\ell}+1}|n_{\ell}+1\rangle.$$

They allow transitions between Fock states by lowering or raising the photon number in mode ℓ by one unit. The vacuum state $|0_{\ell}\rangle$ is annihilated by \hat{a}_{ℓ} , satisfying $\hat{a}_{\ell}|0_{\ell}\rangle = 0$. Thus, the Hamiltonian for the electromagnetic field becomes a sum of harmonic oscillator energies:

$$\hat{H} = \sum_{\ell} \hbar\omega_{\ell} \hat{a}_{\ell}^{\dagger} \hat{a}_{\ell} \quad (\text{II.2})$$

where we ignore the constant zero-point energy term $\frac{1}{2}\hbar\omega_\ell$ for simplicity.

In the following parts, we will always focus on a single mode of the electromagnetic field unless stated otherwise (for the mode matching part), which is sufficient to illustrate the concepts of quantum optics and optomechanics. The generalization to multiple modes is straightforward and follows the same principles. The electric field operator is then written

$$\hat{\mathbf{E}}(\mathbf{r}, t) = i\mathcal{E}_0 \left[\hat{a} \mathbf{f}(\mathbf{r}) e^{-i\omega_0 t} - \hat{a}^\dagger \mathbf{f}^*(\mathbf{r}) e^{+i\omega_0 t} \right]. \quad (\text{II.3})$$

Quadrature Operators

We describe the phase-space properties of a field mode using hermitian quadrature operators. These are linear combinations of the annihilation and creation operators that correspond to measurable observables in the electromagnetic field. The two most common quadratures are defined as follows:

$$\hat{\mathbf{a}} \equiv \begin{pmatrix} \hat{a}_1 \\ \hat{a}_2 \end{pmatrix} = \boldsymbol{\Gamma} \hat{\mathbf{u}}, \quad \boldsymbol{\Gamma} \equiv \begin{pmatrix} 1 & 1 \\ -i & i \end{pmatrix}, \quad \hat{\mathbf{u}} \equiv \begin{pmatrix} \hat{a} \\ \hat{a}^\dagger \end{pmatrix} \quad (\text{II.4})$$

where we defined the field vector $\hat{\mathbf{u}}$ and the transfer matrix $\boldsymbol{\Gamma}$, later used to switch from One-Photon to Two-Photon description of optical elements. In components, we then have $\hat{a}_1 = \hat{a}^\dagger + \hat{a}$ and $\hat{a}_2 = i(\hat{a}^\dagger - \hat{a})$. The matrix form commutator reads

$$[\hat{\mathbf{u}}, \hat{\mathbf{u}}^\dagger] = \sigma_z, \quad (\text{II.5})$$

with σ_z the Pauli Z matrix. An arbitrary rotated quadrature pair is obtained by

$$\hat{\mathbf{a}}_\phi \equiv \begin{pmatrix} \hat{a}_\phi \\ \hat{a}_{\phi+\pi/2} \end{pmatrix} = \mathbf{R}(\phi) \hat{\mathbf{a}} = \mathbf{R}(\phi) \boldsymbol{\Gamma} \hat{\mathbf{u}}, \quad \mathbf{R}(\phi) \equiv \begin{pmatrix} \cos \phi & \sin \phi \\ -\sin \phi & \cos \phi \end{pmatrix}. \quad (\text{II.6})$$

We notice than

$$\mathbf{R}(\phi) \boldsymbol{\Gamma} = \begin{pmatrix} \cos \phi & \sin \phi \\ -\sin \phi & \cos \phi \end{pmatrix} \begin{pmatrix} 1 & 1 \\ -i & i \end{pmatrix} = \begin{pmatrix} e^{-i\phi} & e^{i\phi} \\ -i e^{-i\phi} & i e^{i\phi} \end{pmatrix}. \quad (\text{II.7})$$

so that in components we have

$$\begin{aligned} \hat{a}_\phi &= \hat{a}_1 \cos \phi + \hat{a}_2 \sin \phi = \hat{a} e^{-i\phi} + \hat{a}^\dagger e^{+i\phi} \\ \hat{a}_{\phi+\pi/2} &= -\hat{a}_1 \sin \phi + \hat{a}_2 \cos \phi = i(\hat{a}^\dagger e^{+i\phi} - \hat{a} e^{-i\phi}). \end{aligned} \quad (\text{II.8})$$

The commutators of the rotated quadrature operators read

$$\begin{aligned}
 [\hat{\mathbf{a}}_\phi, \hat{\mathbf{a}}_\phi^\dagger] &= \mathbf{R}(\phi) \mathbf{\Gamma} [\hat{\mathbf{u}}, \hat{\mathbf{u}}^\dagger] \mathbf{\Gamma}^\dagger \mathbf{R}^\dagger(\phi) \\
 &= \mathbf{R}(\phi) \mathbf{\Gamma} \sigma_z \mathbf{\Gamma}^\dagger \mathbf{R}^\dagger(\phi) \\
 &= 2i \mathbf{R}(\phi) \mathbf{J} \mathbf{R}^\dagger(\phi) \\
 &= 2i \mathbf{J},
 \end{aligned} \tag{II.9}$$

where \mathbf{J} is the symplectic form defined as

$$\mathbf{J} \equiv \begin{pmatrix} 0 & 1 \\ -1 & 0 \end{pmatrix}. \tag{II.10}$$

Note that since $\hat{\mathbf{a}}_\phi$ is hermitian, we have $\hat{\mathbf{a}}_\phi^\dagger = \hat{\mathbf{a}}_\phi^T$, and similarly $\mathbf{R}^\dagger(\phi) = \mathbf{R}^T(\phi)$ since all its entries are real.

This compact vector form will be used later for the one- and two-photon description of the light field behaviours in optomechanical systems with squeezed light input.

Note: notes the fact that these are defined for a specific ℓ , so at each mode is associated such a quadrature vector. The multimode treatment is used by the multimode quantum optics community, notably to describe multimode non gaussian states, hidden squeezing (beyond homodyne detection correlations, Patera and co)

Linearization of the optical field

The annihilation operator can be decomposed as

$$\begin{aligned}
 \hat{a} &= \langle \hat{a} \rangle + \delta \hat{a} \\
 &= \bar{\alpha} + \delta \hat{a}
 \end{aligned} \tag{II.11}$$

where $\langle \hat{a} \rangle = \bar{\alpha} \in \mathbb{C}$ is the mean complex amplitude of the quantum state, and $\delta \hat{a}$ represents quantum fluctuations with $\langle \delta \hat{a} \rangle = 0$. Note this decomposition is valid for any quantum state, including coherent and squeezed states. We note $\bar{\alpha}$ to distinguish it from the complex amplitude α of a coherent state introduced below, which is a specific case of this decomposition. The associated matrix form is

$$\hat{\mathbf{u}} = \begin{pmatrix} \bar{\alpha} \\ \bar{\alpha}^* \end{pmatrix} + \begin{pmatrix} \delta \hat{a} \\ \delta \hat{a}^\dagger \end{pmatrix} = \bar{\mathbf{u}} + \delta \hat{\mathbf{u}} \tag{II.12}$$

and it then follows that the quadrature operators can also be expressed as

$$\begin{aligned}\hat{\mathbf{a}}_\phi &= \mathbf{R}(\phi) \boldsymbol{\Gamma} (\bar{\mathbf{u}} + \delta\hat{\mathbf{u}}) \\ &= \bar{\mathbf{a}}_\phi + \delta\hat{\mathbf{a}}_\phi\end{aligned}\quad (\text{II.13})$$

where the fluctuations retain the canonical commutation relations

$$[\delta\hat{\mathbf{u}}, \delta\hat{\mathbf{u}}^\dagger] = \sigma_{\mathbf{z}} \quad \Rightarrow \quad [\delta\hat{\mathbf{a}}_\phi, \delta\hat{\mathbf{a}}_\phi^T] = 2i \mathbf{J}. \quad (\text{II.14})$$

Note: notes on first and second moments, as well as beyond second moments correlations and their use i.e. when and why is this linearization ok to use etc etc

Heisenberg Uncertainty Relation

The covariance of Hermitian operators \hat{A} and \hat{B} is defined as

$$\text{Cov}(\hat{A}, \hat{B}) = \frac{1}{2} \langle \{\delta\hat{A}, \delta\hat{B}\} \rangle \quad (\text{II.15})$$

such that it reduces to the variance δA^2 if $\hat{A} = \hat{B}$. Considering the quadrature operators, we define the covariance matrix as

$$\mathbf{V}_\phi \equiv \frac{1}{2} \langle \{\delta\hat{\mathbf{a}}_\phi, \delta\hat{\mathbf{a}}_\phi^T\} \rangle = \begin{pmatrix} \langle \delta\hat{a}_\phi^2 \rangle & \text{Cov}(\hat{a}_\phi, \hat{a}_{\phi+\pi/2}) \\ \text{Cov}(\hat{a}_\phi, \hat{a}_{\phi+\pi/2}) & \langle \delta\hat{a}_{\phi+\pi/2}^2 \rangle \end{pmatrix} \quad (\text{II.16})$$

and the Heisenberg uncertainty relation reads as

$$\det \mathbf{V}_\phi \geq 1 \quad \Rightarrow \quad \langle \delta\hat{a}_\phi^2 \rangle \langle \delta\hat{a}_{\phi+\pi/2}^2 \rangle - \text{Cov}^2(\hat{a}_\phi, \hat{a}_{\phi+\pi/2}) \geq 1 \quad (\text{II.17})$$

Graphical Representation of Gaussian States

For Gaussian states, we can actually picture them in a 2D space, where ...

II.1.2 Coherent and Squeezed States

We now turn to standard optical quantum states, in particular gaussian states i.e. full positive in Wigner function representations such as coherent and squeezed states, that we will denote in braket notation as $|\alpha\rangle$ and $|\alpha, r, \theta\rangle$.

Coherent States:

The coherent state $|\alpha\rangle$ is an eigenstate of the annihilation operator:

$$\hat{a} |\alpha\rangle = \alpha |\alpha\rangle \quad (\text{II.18})$$

where $\alpha = |\alpha|e^{i\bar{\varphi}}$ is a complex number representing the mean coherent amplitude. In this notation, the angle $\bar{\varphi}$ is the mean angle of the distribution, used to describe the relative phase to a reference (e.g. a local oscillator), as in Fig ???. The \hat{a} linear decomposition above (Eq (II.11)) then yields $\alpha = \bar{\alpha}$ for a coherent state. It can be expressed in the Fock basis as

$$|\alpha\rangle = e^{-|\alpha|^2/2} \sum_{n=0}^{\infty} \frac{\alpha^n}{\sqrt{n!}} |n\rangle \quad (\text{II.19})$$

and are generated by the action of the displacement operator $\hat{D}(\alpha)$ on the vacuum state $|0\rangle$:

$$|\alpha\rangle = \hat{D}(\alpha) |0\rangle, \quad \hat{D}(\alpha) = \exp(\alpha\hat{a}^\dagger - \alpha^*\hat{a}) \quad (\text{II.20})$$

Note: note on the convention used i.e. $\alpha \neq \bar{\alpha}$, $\alpha_0 \neq \bar{\alpha}_0$

Expectation values of quadrature operators

Using the quadrature vector $\hat{\mathbf{a}}_\phi$ (Eq II.6), the expectation values in a coherent state are

$$\langle \hat{\mathbf{a}}_\phi \rangle = \mathbf{R}(\phi) \langle \hat{\mathbf{a}} \rangle = 2 \begin{pmatrix} \text{Re}(\alpha e^{-i\phi}) \\ \text{Im}(\alpha e^{-i\phi}) \end{pmatrix} \quad (\text{II.21})$$

such that the components reduce to $2\text{Re}(\alpha)$ and $2\text{Im}(\alpha)$ if $\phi = 0$.

Amplitude and phase quadratures

It is convenient to introduce the amplitude-phase quadrature vector at $\phi = \bar{\varphi}$

$$\hat{\mathbf{a}}_{\bar{\varphi}} = \begin{pmatrix} \hat{p} \\ \hat{q} \end{pmatrix} = \begin{pmatrix} \hat{a}_{\bar{\varphi}} \\ \hat{a}_{\bar{\varphi}+\pi/2} \end{pmatrix}. \quad (\text{II.22})$$

with expectation values

$$\langle \hat{\mathbf{a}}_{\bar{\varphi}} \rangle = 2 \begin{pmatrix} |\alpha| \\ 0 \end{pmatrix}, \quad (\text{II.23})$$

Covariance matrix

For a coherent state, fluctuations are vacuum-like:

$$\delta\hat{a}_\phi^2 = \delta\hat{a}_{\phi+\pi/2}^2 = 1, \quad \text{Cov}(\hat{a}_\phi, \hat{a}_{\phi+\pi/2}) = 0, \quad (\text{II.24})$$

so that

$$\mathbf{V}_\phi = \begin{pmatrix} 1 & 0 \\ 0 & 1 \end{pmatrix} = \mathbb{I}_2, \quad \forall \phi. \quad (\text{II.25})$$

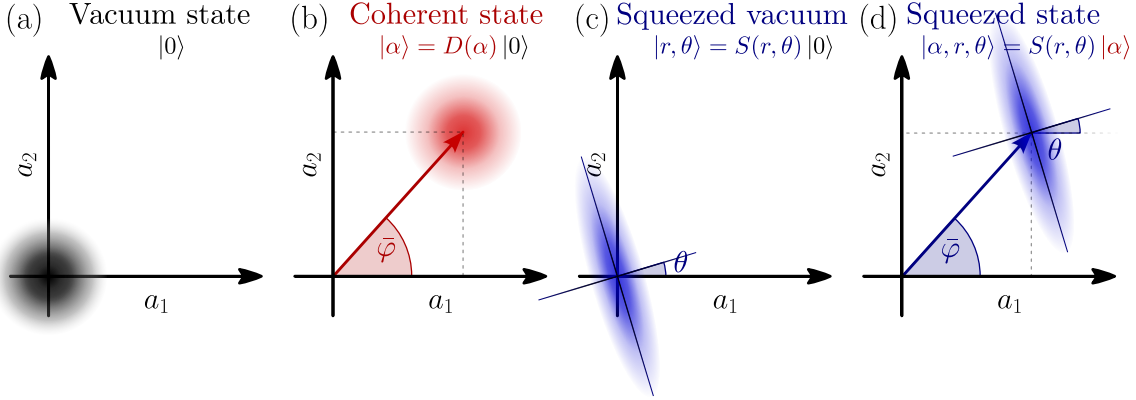


Fig. II.1 Phase-space representations of quantum states and transformations. (a) Wigner function of the vacuum state: a circular Gaussian centered at the origin, representing equal quantum fluctuations in both quadratures a_1 and a_2 . (b) Wigner function of a coherent state: a displaced circular Gaussian, showing a shift in phase space along an angle φ with unchanged, isotropic noise. (c) Wigner function of a squeezed vacuum state: an elliptical Gaussian centered at the origin, with reduced noise along a rotated quadrature X_θ and increased noise in the orthogonal direction. (d) Wigner function of a displaced squeezed state: an ellipse shifted away from the origin, combining anisotropic fluctuations and a nonzero mean amplitude. The displacement angle φ and squeezing angle θ are independent.

This saturates the Heisenberg uncertainty relation $\det \mathbf{V}_\phi = 1$ in the units defined here i.e. it is a minimum uncertainty state.

Photon number statistics

The mean and variance of the photon number operator $\hat{N} = \hat{a}^\dagger \hat{a}$ are

$$\langle \hat{N} \rangle = |\alpha|^2, \quad \Delta N^2 = |\alpha|^2. \quad (\text{II.26})$$

That is, coherent states display Poissonian photon statistics.

Squeezed States:

Squeezed states $|\alpha, r, \theta\rangle$ are quantum gaussian states of light in which the noise (variance) of one quadrature is reduced below the vacuum level, at the expense of increased noise in the conjugate quadrature. The single-mode squeezed vacuum state is defined as

$$|0, r, \theta\rangle = \hat{S}(r, \theta)|0\rangle, \quad \hat{S}(\theta) = \exp \left[\frac{r}{2} (e^{-2i\theta} \hat{a}^2 - e^{-2i\theta} \hat{a}^{\dagger 2}) \right] \quad (\text{II.27})$$

where r is the squeezing parameter (strength) and θ is the squeezing angle i.e. the angle along which one quadrature is reduced below vacuum level. The most general Gaussian state is the displaced squeezed state, obtained by applying both the squeezing operator $\hat{S}(r, \theta)$ and the displacement operator $\hat{D}(\alpha)$ to the vacuum:

$$|\alpha, r, \theta\rangle = \hat{S}(r, \theta)\hat{D}(\alpha)|0\rangle \quad (\text{II.28})$$

where $\hat{D}(\alpha)$ displaces the state in phase space by the complex amplitude α , defined similarly to the coherent state.

Note: The displacement and squeezing operators do not commute, i.e. $\hat{D}(\alpha)\hat{S}(r, \theta) \neq \hat{S}(r, \theta)\hat{D}(\alpha)$. However, both orderings correspond to experimentally valid procedures: one can either squeeze the vacuum and then displace (e.g. by mixing with a coherent state on a beamsplitter), or squeeze a coherent state straight away (e.g. by seeding an optical parametric amplifier). The resulting state is always a displaced squeezed state, but the relative phase between displacement and squeezing may differ.

Expectation values of quadrature operators

Using the usual quadratures defined in Eq (II.4) and (II.6), the expectation values in a displaced squeezed state are

$$\langle \hat{\mathbf{a}} \rangle = 2 \begin{pmatrix} \text{Re } \alpha \\ \text{Im } \alpha \end{pmatrix}, \quad \langle \hat{\mathbf{a}}_\phi \rangle = 2 \begin{pmatrix} \text{Re } (\alpha e^{-i\phi}) \\ \text{Im } (\alpha e^{-i\phi}) \end{pmatrix}. \quad (\text{II.29})$$

For a squeezed vacuum ($\alpha = 0$) all quadrature means vanish.

Quadrature aligned with the squeezing axis to rewrite

Choosing $\phi = \theta$ yields

$$\langle \delta \hat{a}_\theta^2 \rangle = e^{-2r}, \quad \langle \delta \hat{a}_{\theta+\pi/2}^2 \rangle = e^{2r}, \quad \text{Cov}(\hat{a}_\theta, \hat{a}_{\theta+\pi/2}) = 0, \quad (\text{II.30})$$

with uncertainty product $\Delta \hat{a}_\theta \Delta \hat{a}_{\theta+\pi/2} = 1$ saturating the Heisenberg bound. The corresponding mean vector is

$$\langle \hat{\mathbf{a}}_\theta \rangle = 2 \begin{pmatrix} \text{Re } (\alpha e^{-i\theta}) \\ \text{Im } (\alpha e^{-i\theta}) \end{pmatrix}. \quad (\text{II.31})$$

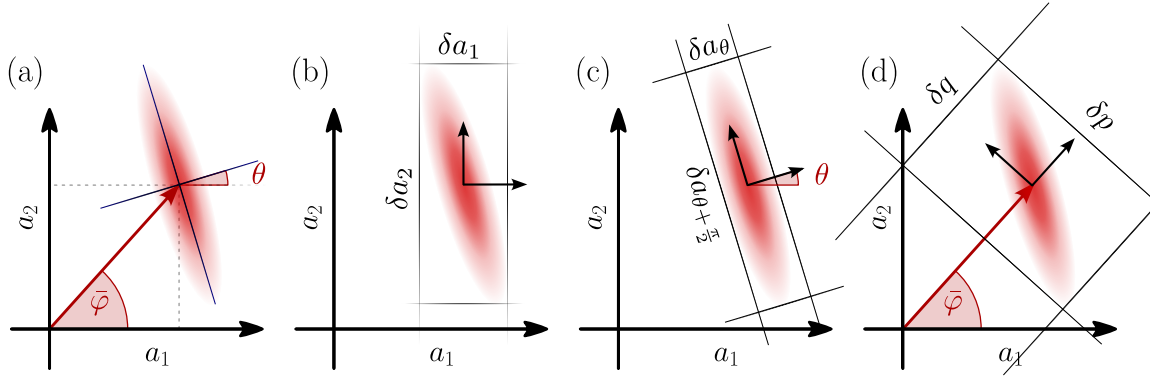


Fig. II.2 Phase-space representations of quantum states and transformations. (a) Wigner function of the vacuum state: a circular Gaussian centered at the origin, representing equal quantum fluctuations in both quadratures X_1 and X_2 . (b) Wigner function of a coherent state: a displaced circular Gaussian, showing a shift in phase space along an angle φ with unchanged, isotropic noise. (c) Wigner function of a squeezed vacuum state: an elliptical Gaussian centered at the origin, with reduced noise along a rotated quadrature X_θ and increased noise in the orthogonal direction. (d) Wigner function of a displaced squeezed state: an ellipse shifted away from the origin, combining anisotropic fluctuations and a nonzero mean amplitude. The displacement angle φ and squeezing angle θ are independent.

Covariance matrix

Let $\psi \equiv \phi - \theta$ be the measurement angle ϕ relative to the squeezing axis θ . For a displaced squeezed state, the covariance matrix is

$$\mathbf{V}_\phi = \mathbf{R}(\psi) \begin{pmatrix} e^{-2r} & 0 \\ 0 & e^{2r} \end{pmatrix} \mathbf{R}(\psi)^T. \quad (\text{II.32})$$

Expanding this explicitly gives

$$\mathbf{V}_\phi = \begin{pmatrix} e^{-2r} \cos^2 \psi + e^{2r} \sin^2 \psi & \frac{1}{2} \sin 2\psi (e^{2r} - e^{-2r}) \\ \frac{1}{2} \sin 2\psi (e^{2r} - e^{-2r}) & e^{-2r} \sin^2 \psi + e^{2r} \cos^2 \psi \end{pmatrix}. \quad (\text{II.33})$$

The covariance term is therefore

$$\text{Cov}(\hat{a}_\phi, \hat{a}_{\phi+\pi/2}) = \frac{1}{2} \sin 2(\phi - \theta) (e^{2r} - e^{-2r}), \quad (\text{II.34})$$

which vanishes when $\sin 2(\phi - \theta) = 0$, i.e.

$$\phi - \theta \in \left\{ 0, \frac{\pi}{2}, \pi, \dots \right\}.$$

Along these principal axes of squeezing, \mathbf{V}_ϕ is diagonal.

Amplitude and Phase squeezed states

Considering a displaced squeezed state, two special cases are of interest: the amplitude squeezed state where $\theta = \bar{\varphi}$ and the phase squeezed state where $\theta = \bar{\varphi} + \pi/2$. In the first case, the amplitude quadrature \hat{p} is squeezed, while the phase quadrature \hat{q} is anti-squeezed. In the second case, the phase quadrature is squeezed, while the amplitude quadrature is anti-squeezed. The covariance matrices for these states can be derived from Eq. (II.32) by setting $\psi = 0$ or $\psi = \pi/2$, respectively.

Photon number statistics

The mean and variance of the photon number operator $\hat{N} = \hat{a}^\dagger \hat{a}$ in a displaced squeezed state are

$$\langle \hat{N} \rangle = |\alpha|^2 + \sinh^2 r, \quad \Delta N^2 = |\alpha|^2 \cosh 2r + \frac{1}{2} \sinh^2 2r. \quad (\text{II.35})$$

to rewrite This shows that the squeezing operation increases the mean photon number of the coherent state by adding photons. Physically, this reflects the fact that generating squeezed light requires injecting energy into the system, so the squeezed vacuum contains correlated field excitations (photons) in even numbers. This is further seen by examining the photon-number distribution P_n : for a squeezed vacuum only even n occur, while displacement progressively repopulates the odd n and shifts weight to higher n , in agreement with the increase of $\langle \hat{N} \rangle$ and ΔN^2 above.

II.1.3 Sidebands and Quantum Noises

Modulation picture

In realistic optical systems, the electromagnetic field is never perfectly monochromatic, nor isolated from its environment, nor static through time. Instead, it exhibits a finite spectral linewidth (stimulated emission, phase noise etc...), as well as non intentional/intentional modulations, all imprinted onto the carrier field. These effects cause the field amplitude and phase to evolve slowly compared to the optical frequency ω_0 .

As a result, the complex amplitude associated with each mode and described by the Schrodinger-picture annihilation operator \hat{a} , acquires an explicit time dependence beyond the standard fast-oscillating term $e^{-i\omega_0 t}$. It is often quoted as *modulation* picture in the litterature. We then promote the field vector to

$$\hat{\mathbf{u}} = \bar{\mathbf{u}} + \delta \hat{\mathbf{u}} \quad \rightarrow \quad \hat{\mathbf{u}}(t) = \bar{\mathbf{u}}(t) + \delta \hat{\mathbf{u}}(\mathbf{t}) \quad (\text{II.36})$$

where the canonical commutation relations given in equation (II.14) becomes:

$$[\delta\hat{\mathbf{u}}(t), \delta\hat{\mathbf{u}}(t')^\dagger] = \sigma_{\mathbf{z}} \delta(t - t'). \quad (\text{II.37})$$

and the covariance matrix of the ammplitude-phase quadratures turns to

$$\mathbf{V}(t, t') = \begin{pmatrix} \langle \delta\hat{p}(t)\delta\hat{p}(t') \rangle & \text{Cov}(\hat{p}(t), \hat{q}(t')) \\ \text{Cov}(\hat{q}(t), \hat{p}(t')) & \langle \delta\hat{q}(t)\delta\hat{q}(t') \rangle \end{pmatrix} \delta(t - t') \quad (\text{II.38})$$

This time dependence allows us to track both slow classical modulations of the field $\bar{\mathbf{u}}(t)$ and the intrinsic quantum fluctuations $\delta\hat{\mathbf{u}}(t)$. Note this is equivalent to the interaction picture where the reference angular frequency would be ω_0 , but where we also consider dynamical processes way slower than this frequency. Additionally, we will always consider the limit of weak fluctuations, where the quantum noise can be treated perturbatively around the classical field i.e.

$$|\bar{\alpha}(t)| \gg \Delta\hat{a}_\theta(t)$$

The resulting field operator can then be expressed as a

$$\begin{aligned} \hat{\mathbf{E}}(\mathbf{r}, t) = i\mathcal{E}_0 & \left[[\alpha(t) \mathbf{f}(\mathbf{r}) e^{-i\omega_0 t} - \alpha^*(t) \mathbf{f}^*(\mathbf{r}) e^{i\omega_0 t}] \right. \\ & \left. + [\delta\hat{a}(t) \mathbf{f}(\mathbf{r}) e^{-i\omega_0 t} - \delta\hat{a}^\dagger(t) \mathbf{f}^*(\mathbf{r}) e^{i\omega_0 t}] \right] \end{aligned} \quad (\text{II.39})$$

Fourier Domain & Sidebands

To deal with noise spectra, we need to rewrite the various quadratures defined in the previous sections in the Fourier domain, where each frequency component is called a *sideband*.

The Fourier transform of the field vector is defined as

$$\begin{aligned} \hat{\mathbf{u}}[\Omega] &= \int_{-\infty}^{\infty} dt e^{i\Omega t} \hat{\mathbf{u}}(t) \\ \hat{\mathbf{u}}(t) &= \frac{1}{2\pi} \int_{-\infty}^{\infty} d\Omega e^{-i\Omega t} \hat{\mathbf{u}}[\Omega] \end{aligned} \quad (\text{II.40})$$

where $\Omega \ll \omega_0$ is the sideband frequency relative to the so called *carrier* frequency ω_0 . Add something on the true integral bound i.e. bandwidth B In this definition, a notable property is that the hermitian conjugate in the time domain translates to a frequency inversion in the Fourier domain:

$$[\hat{a}(t)]^\dagger = \hat{a}^\dagger(t), \quad [\hat{a}[\Omega]]^\dagger = \hat{a}^\dagger[-\Omega]. \quad (\text{II.41})$$

To lighten the notation we will use $\hat{a}^\dagger[\pm\Omega] = \hat{a}_\pm$. Carrying out the linearization in the

Fourier domain, we have

$$\begin{aligned}\hat{\mathbf{u}}[\Omega] &= \begin{pmatrix} \bar{\alpha}_+ \\ \bar{\alpha}_-^* \end{pmatrix} + \begin{pmatrix} \delta\hat{a}_+ \\ \delta\hat{a}_-^\dagger \end{pmatrix} \\ &= \bar{\mathbf{u}}[\Omega] + \delta\hat{\mathbf{u}}[\Omega]\end{aligned}\quad (\text{II.42})$$

with the fluctuations commutator reading

$$[\delta\hat{\mathbf{u}}[\Omega], \delta\hat{\mathbf{u}}[\Omega']^\dagger] = \sigma_{\mathbf{z}} \delta(\Omega + \Omega'). \quad (\text{II.43})$$

The quadrature operators in the Fourier domain are then written as

$$\begin{aligned}\hat{\mathbf{a}}_\phi[\Omega] &= \mathbf{R}(\phi) \Gamma \bar{\mathbf{u}}[\Omega] + \mathbf{R}(\phi) \Gamma \delta\hat{\mathbf{u}}[\Omega] \\ &= \underbrace{2|\bar{\alpha}| \begin{pmatrix} \cos(\bar{\varphi} - \phi) \\ \sin(\bar{\varphi} - \phi) \end{pmatrix} \delta(\Omega)}_{\text{classical part}} + \underbrace{\begin{pmatrix} \delta\hat{a}_\phi[\Omega] \\ \delta\hat{a}_{\phi+\pi/2}[\Omega] \end{pmatrix}}_{\text{quantum fluctuations}}\end{aligned}\quad (\text{II.44})$$

such that the amplitude-phase quadrature vector reads

$$\hat{\mathbf{a}}_{\bar{\varphi}}[\Omega] = 2|\bar{\alpha}| \begin{pmatrix} 1 \\ 0 \end{pmatrix} \delta(\Omega) + \begin{pmatrix} \delta\hat{p}[\Omega] \\ \delta\hat{q}[\Omega] \end{pmatrix} \quad (\text{II.45})$$

where we have

$$\begin{pmatrix} \delta\hat{p}[\Omega] \\ \delta\hat{q}[\Omega] \end{pmatrix} = \begin{pmatrix} \delta\hat{a}_+ + \delta\hat{a}_-^\dagger \\ i(\delta\hat{a}_-^\dagger - \delta\hat{a}_+) \end{pmatrix} \quad (\text{II.46})$$

This very way of writing the field quadratures is known as the *two-photon* formalism, introduced by Caves and Schumaker [?, ?]. Here, we wrote down a vector, linearized form, useful to compute spectra numerically (see section ??). Throughout the litterature, the amplitude-phase two-photon quadratures are called differently, namely (a_I, a_Q) (Caves and Schumaker), (X_1, X_2) (Gerry and Knight), (X, Y) (Bachor and Ralph) or (x, p) (Weedbrook et al.). We chose the p, q convention to perpetuate the convention used at LKB.

Note: In the modulation picture, fluctuations in the time domain appear as symmetric sidebands at $+\Omega$ and $-\Omega$. Any experimentally accessible, real signal arises from the interference of these two sidebands (quadratures in homodyne detection, intensity fluctuations, photocurrent spectra); equivalently, Hermiticity in time forces Fourier components to couple $+\Omega$ with $-\Omega$. Packaging the field as the two-photon vector $(\hat{a}[\Omega], \hat{a}^\dagger[-\Omega])^T$ therefore groups exactly the two degrees of freedom that generate a single measurable fluctuation at frequency Ω . This makes correlations between the sidebands (which are the essence of

frequency-dependent squeezing) explicit and ensures that quadrature spectra remain manifestly real. By contrast, the vector $(\hat{a}[\Omega], \hat{a}^\dagger[\Omega])^T$ is convenient for per-frequency photon-number or passive-scattering calculations, but it obscures the intrinsic pairing required to form real observables, forcing one to carry $-\Omega$ separately. For the noise-spectral analysis pursued here, the sideband-pair representation is thus the phenomenologically natural and algebraically minimal choice.

Amplitude Modulation (AM)

Let the classical amplitude be modulated at Ω_{mod} in amplitude:

$$\alpha(t) = \bar{\alpha} (1 + \epsilon_a \cos(\Omega_{\text{mod}} t)) \quad (\text{II.47})$$

with $\epsilon_a \ll 1$, the field amplitude modulation depth. While the DC term lives at frequency ω_0 , the modulation introduces sidebands at frequencies $\omega_0 \pm \Omega_{\text{mod}}$, seen by expanding the cosine:

$$\alpha(t) = \bar{\alpha} \left(1 + \frac{\epsilon_a}{2} e^{i\Omega_{\text{mod}} t} + \frac{\epsilon_a}{2} e^{-i\Omega_{\text{mod}} t} \right) \quad (\text{II.48})$$

Phase Modulation (PM)

Let the classical amplitude be modulated in phase at frequency Ω_{mod} :

$$\alpha(t) = \bar{\alpha} e^{i\epsilon_\phi \cos(\Omega_{\text{mod}} t)} \quad (\text{II.49})$$

with $\epsilon_\phi \ll 1$ the field phase modulation depth. Expanding to first order in ϵ_ϕ gives:

$$\alpha(t) \approx \bar{\alpha} \left(1 + \frac{i\epsilon_\phi}{2} e^{i\Omega_{\text{mod}} t} + \frac{i\epsilon_\phi}{2} e^{-i\Omega_{\text{mod}} t} \right) \quad (\text{II.50})$$

While the carrier term lives at frequency ω_0 , the modulation introduces sidebands at $\omega_0 \pm \Omega_{\text{mod}}$, both shifted in phase by $\pi/2$ relative to the carrier.

Linearized Hermitian Operators

In both cases, the field contains a carrier at frequency ω and two sidebands at $\omega \pm \Omega$. Amplitude modulation results in sidebands that are in phase with the carrier, while phase modulation produces sidebands with a $\pm\pi/2$ phase shift relative to the carrier. We also note a general modulation process as :

$$\alpha(t) = \bar{\alpha} (1 + \varepsilon(t)) \quad (\text{II.51})$$

where $\varepsilon(t) \in \mathbb{C}$ is a modulation function that weakly modulates the complex amplitude in time, and that features information about the modulation frequency and depth. It then follows that the linearized amplitude-phase operators can be expressed as

$$\hat{\mathbf{a}}_{\bar{\varphi}}(t) = 2|\bar{\alpha}| \begin{pmatrix} 1 \\ 0 \end{pmatrix} + 2|\bar{\alpha}| \begin{pmatrix} \text{Re}(\varepsilon(t)) \\ \text{Im}(\varepsilon(t)) \end{pmatrix} + \begin{pmatrix} \delta\hat{p}(t) \\ \delta\hat{q}(t) \end{pmatrix} \quad (\text{II.52})$$

And the quadrature operators can be expressed as

$$\hat{\mathbf{a}}_{\bar{\varphi}}[\Omega] = 2|\bar{\alpha}| \begin{pmatrix} 1 \\ 0 \end{pmatrix} \delta(\Omega) + 2|\bar{\alpha}| \begin{pmatrix} \text{Re}(\varepsilon[\Omega]) \\ \text{Im}(\varepsilon[\Omega]) \end{pmatrix} + \begin{pmatrix} \delta\hat{p}[\Omega] \\ \delta\hat{q}[\Omega] \end{pmatrix} \quad (\text{II.53})$$

Computing the Fourier transform for amplitude and phase modulations yields

$$\begin{aligned} \varepsilon^{AM}(\Omega) &= \frac{\epsilon_a}{2} \left(\delta(\Omega - \Omega_{\text{mod}}) + \delta(\Omega + \Omega_{\text{mod}}) \right) \\ \varepsilon^{PM}(\Omega) &= \frac{i\epsilon_\phi}{2} \left(\delta(\Omega - \Omega_{\text{mod}}) + \delta(\Omega + \Omega_{\text{mod}}) \right) \end{aligned} \quad (\text{II.54})$$

Noise Spectra

We now introduce the cross spectra matrix for two arbitrary linearized hermitian operators $\hat{A} = \bar{A} + \delta\hat{A}$ and $\hat{B} = \bar{B} + \delta\hat{B}$, which describes their correlations at different frequencies. It is defined as

$$\mathbf{S}_{AB}(\Omega) = \begin{pmatrix} S_{AA}(\Omega) & S_{AB}(\Omega) \\ S_{BA}(\Omega) & S_{BB}(\Omega) \end{pmatrix} \quad (\text{II.55})$$

where

$$S_{AB}(\Omega) = \frac{1}{2\pi} \int \delta\Omega' \langle \delta\hat{A}(\Omega), \delta\hat{B}(\Omega') \rangle \quad (\text{II.56})$$

is the two-sided cross spectrum between \hat{A} and \hat{B} . In our way of writing it, we include all time dependent processes inside de fluctuation operators i.e. $\varepsilon(t)$ and $\delta\hat{p}(t)$, $\delta\hat{q}(t)$ in the case of quadrature operators, as all terms in $\delta(\Omega)$ contribute to the DC part of the spectrum. We illustrate this by computing the diagonal elements of the amplitude-phase quadrature of a coherent field modulated in amplitude. The amplitude-phase quadrature fluctuation part reads

$$\delta\hat{\mathbf{a}}_{\bar{\varphi}}[\Omega] = |\bar{\alpha}| \epsilon_a \begin{pmatrix} \delta(\Omega - \Omega_{\text{mod}}) + \delta(\Omega + \Omega_{\text{mod}}) \\ 0 \end{pmatrix} + \begin{pmatrix} \delta\hat{p}[\Omega] \\ \delta\hat{q}[\Omega] \end{pmatrix} \quad (\text{II.57})$$

and its amplitude and phase noise spectra are

$$\begin{aligned} S_{pp}(\Omega) &= 2|\bar{\alpha}|^2 \epsilon_a^2 \left(\delta(\Omega - \Omega_{\text{mod}}) + \delta(\Omega + \Omega_{\text{mod}}) \right) + 1 \\ S_{qq}(\Omega) &= 1 \end{aligned} \quad (\text{II.58})$$

II.1.4 Quantum Sideband Diagram

As seen in the above expression for the amplitude and phase spectra for a amplitude modulated coherent state, the two-sided spectra display a sum of dirac functions corresponding to classical modulations of the field, as well as a flat quantum noise across all frequencies, as coherent state feature vacuum like fluctuations at all frequencies. In the mean time, the summation of the Ω' frequencies in Eq (II.56) captures the two-photon correlations defined in Eq (II.46). To graphically display this phenomenology, we resort to the so called *Quantum Sideband* diagram, which is an extension of the phase space representation introduced earlier to the negative and positive sideband frequencies of the carrier field, capturing two-photon correlations between symmetric sidebands.

Starting with the simplest case : the vacuum/coherent state.

II.2 Optical Cavities: Basics

II.2.1 Cavity types and Resonance Conditions

II.2.2 Spatial and Longitudinal Modes

II.2.3 Quantum Langevin Equations

We consider a field cavity mode described by the annihilation operator $\hat{a}(t)$, interacting with several independent noise inputs. The system is governed by a Hamiltonian $\hat{H} = -\hbar\Delta a^\dagger a$ with $\Delta \equiv \omega_0 - \omega_c$ the cavity detuning to the laser frequency, and each input introduces dissipation characterized by a decay rate $\kappa_i = T_i/\tau$, with T_i the power transmittivity of the mirror and $\tau = 2L/c$ the roundtrip time of the cavity. This is we consider an input coupler (mirror) with decay rate κ_1 and an output coupler (mirror) with decay rate κ_2 . The laser field is shone onto the cavity by the input coupler. In the modulation picture, the dynamics of \hat{a} is given by the quantum Langevin equation:

$$\begin{aligned}\frac{d}{dt}\hat{a}(t) &= -\frac{i}{\hbar}[\hat{a}, \hat{H}] - \frac{\kappa}{2}\hat{a}(t) + \sqrt{\kappa_1}\hat{a}_{\text{in}}(t) + \sqrt{\kappa_2}\delta\hat{a}_{\text{vac}}(t) \\ &= -\left(\frac{\kappa}{2} - i\Delta\right)\hat{a}(t) + \sqrt{\kappa_1}\hat{a}_{\text{in}}(t) + \sqrt{\kappa_2}\delta\hat{a}_{\text{vac}}(t)\end{aligned}\quad (\text{II.59})$$

where $\kappa = \kappa_0 + \kappa_1 + \kappa_2$ is the total decay rate, with $\kappa_0 = \gamma/\tau$ additional losses. Another key element to deriving both steady state behaviour as well as quadrature spectra is the input-output formula given by $\hat{a}_{\text{out}} = \sqrt{\kappa_{\text{out}}}\hat{a} - \hat{a}_{\text{in}}$ which, in our two coupler system, gives us :

$$\hat{a}_{\text{ref}} = \sqrt{\kappa_1}\hat{a} - \hat{a}_{\text{in}}, \quad \hat{a}_{\text{trans}} = \sqrt{\kappa_2}\hat{a} - \delta\hat{a}_{\text{vac}} \quad (\text{II.60})$$

for both the reflected and transmitted field. In the input-output formula, the \hat{a}_{in} refers to the field incoming on the coupler considered, which are simple vacuum fluctuations on the output coupler since we don't shine the laser by this port.

As introduced in the previous subsection, one can split the annihilation operator in a mean field part α and a fluctuation part $\delta \hat{\mathbf{u}}(t)$ (vector form) such that this equation turns into two i.e. a scalar differential equation, and an operator differentail equation, that is:

$$\begin{aligned} 0 &= -\left(\frac{\kappa}{2} - i\Delta\right)\bar{\alpha} + \sqrt{\kappa_1}\bar{\alpha}_{\text{in}} \\ \frac{d}{dt}\delta\hat{\mathbf{u}}(t) &= -\begin{pmatrix} \frac{\kappa}{2} - i\Delta & 0 \\ 0 & \frac{\kappa}{2} + i\Delta \end{pmatrix}\delta\hat{\mathbf{u}}(t) + \sqrt{\kappa_1}\delta\hat{\mathbf{u}}_{\text{in}}(t) + \sqrt{\kappa_2}\delta\hat{\mathbf{u}}_{\text{vac}}(t) \end{aligned} \quad (\text{II.61})$$

Steady state solution

Taking the first scalar equation and expressing the mean intracavity field gives

$$\bar{\alpha} = \frac{\sqrt{\kappa_1}}{\left(\kappa/2 - i\Delta\right)}\bar{\alpha}_{\text{in}} \quad (\text{II.62})$$

Patching it up with the input-output formula this gives

$$\bar{\alpha}_{\text{ref}} = \left(\frac{\kappa_1}{\kappa/2 - i\Delta} - 1\right)\bar{\alpha}_{\text{in}}, \quad \bar{\alpha}_{\text{trans}} = \frac{\sqrt{\kappa_1\kappa_2}}{\left(\kappa/2 - i\Delta\right)}\bar{\alpha}_{\text{in}}. \quad (\text{II.63})$$

The reflection and transmission coefficients are then

$$R(\Delta) = \left|\frac{\bar{\alpha}_{\text{ref}}}{\bar{\alpha}_{\text{in}}}\right|^2 = \left|\frac{\kappa_1}{\kappa/2 - i\Delta} - 1\right|^2 = \frac{(\kappa_1 - \kappa/2)^2 + \Delta^2}{(\kappa/2)^2 + \Delta^2}, \quad (\text{II.64})$$

$$T(\Delta) = \left|\frac{\bar{\alpha}_{\text{trans}}}{\bar{\alpha}_{\text{in}}}\right|^2 = \frac{\kappa_1\kappa_2}{(\kappa/2)^2 + \Delta^2}. \quad (\text{II.65})$$

Plugging back the expression of $\kappa_i = T_i/\tau$ in the reflection coefficient, we have

$$R(\pm\infty) = 1, \quad R(0) = \left(\frac{T_1 - T_2 - \gamma}{T_1 + T_2 + \gamma}\right)^2 \quad (\text{II.66})$$

Noise Spectra

To derive the spectra we go to Fourier space such that

$$\mathbf{M}_\Delta \delta\hat{\mathbf{u}}[\Omega] = \sqrt{\kappa_1}\delta\hat{\mathbf{u}}_{\text{in}}[\Omega] + \sqrt{\kappa_2}\delta\hat{\mathbf{u}}_{\text{vac}}[\Omega] \quad (\text{II.67})$$

with

$$\mathbf{M}_\Delta = \begin{pmatrix} \frac{\kappa}{2} - i(\Delta + \Omega) & 0 \\ 0 & \frac{\kappa}{2} + i(\Delta - \Omega) \end{pmatrix} \quad (\text{II.68})$$

One can then build the intracavity two-photon quadratures as

$$\boldsymbol{\Gamma} \delta \hat{\mathbf{u}}[\Omega] = \begin{pmatrix} \delta \hat{p}[\Omega] \\ \delta \hat{q}[\Omega] \end{pmatrix} = \sqrt{\kappa_1} \boldsymbol{\Gamma} \mathbf{M}_\Delta^{-1} \delta \hat{\mathbf{u}}_{\text{in}}[\Omega] + \sqrt{\kappa_2} \boldsymbol{\Gamma} \mathbf{M}_\Delta^{-1} \delta \hat{\mathbf{u}}_{\text{vac}}[\Omega] \quad (\text{II.69})$$

as well as the reflected and transmitted quadratures

$$\begin{pmatrix} \delta \hat{p}_{\text{ref}}[\Omega] \\ \delta \hat{q}_{\text{ref}}[\Omega] \end{pmatrix} = (\kappa_1 \boldsymbol{\Gamma} \mathbf{M}_\Delta^{-1} - \boldsymbol{\Gamma}) \delta \hat{\mathbf{u}}_{\text{in}}[\Omega] + \sqrt{\kappa_1 \kappa_2} \boldsymbol{\Gamma} \mathbf{M}_\Delta^{-1} \delta \hat{\mathbf{u}}_{\text{vac}}[\Omega] \quad (\text{II.70})$$

$$\begin{pmatrix} \delta \hat{p}_{\text{trans}}[\Omega] \\ \delta \hat{q}_{\text{trans}}[\Omega] \end{pmatrix} = \sqrt{\kappa_1 \kappa_2} \boldsymbol{\Gamma} \mathbf{M}_\Delta^{-1} \delta \hat{\mathbf{u}}_{\text{in}}[\Omega] + \kappa_2 \boldsymbol{\Gamma} \mathbf{M}_\Delta^{-1} \delta \hat{\mathbf{u}}_{\text{vac}}[\Omega] \quad (\text{II.71})$$

where the inverse of the \mathbf{M}_Δ matrix is given by

$$\mathbf{M}_\Delta^{-1} = \begin{pmatrix} \frac{\kappa/2 + i(\Delta + \Omega)}{(\kappa/2)^2 + (\Delta + \Omega)^2} & 0 \\ 0 & \frac{\kappa/2 - i(\Delta - \Omega)}{(\kappa/2)^2 + (\Delta - \Omega)^2} \end{pmatrix} \quad (\text{II.72})$$

This equation is the key to understanding the filtering properties of optical cavities. If $\Delta \neq 0$, the matrix product $\boldsymbol{\Gamma} \mathbf{M}_\Delta^{-1}$ feature off diagonal element. This produces reflected fluctuations in our two hermitian observables that are linear superpositions of the + and - sidebands. If not correlated/entangled, this will result in nothing spectacular. However, if the input fluctuations are squeezed, ...

Mode Cleaner

A Mode Cleaner (MC) is frequently used to purify the coherent state incoming onto a cavity from classical noises. It is characterized by a configuration such that $\kappa_1 \approx \kappa_2 \approx \kappa/2$ where we neglect the losses κ_0 . It is locked on resonance ($\Delta = 0$), such that the \mathbf{M}_Δ matrix becomes diagonal, allowing us to write

$$\begin{pmatrix} \delta \hat{p}_{\text{ref}}[\Omega] \\ \delta \hat{q}_{\text{ref}}[\Omega] \end{pmatrix} = (\kappa_1 \boldsymbol{\Gamma} \mathbf{M}_\Delta^{-1} - \boldsymbol{\Gamma}) \delta \hat{\mathbf{u}}_{\text{in}}[\Omega] + \sqrt{\kappa_1 \kappa_2} \boldsymbol{\Gamma} \mathbf{M}_\Delta^{-1} \delta \hat{\mathbf{u}}_{\text{vac}}[\Omega] \quad (\text{II.73})$$

$$\begin{pmatrix} \delta \hat{p}_{\text{trans}}[\Omega] \\ \delta \hat{q}_{\text{trans}}[\Omega] \end{pmatrix} = \sqrt{\kappa_1 \kappa_2} \boldsymbol{\Gamma} \mathbf{M}_\Delta^{-1} \delta \hat{\mathbf{u}}_{\text{in}}[\Omega] + \kappa_2 \boldsymbol{\Gamma} \mathbf{M}_\Delta^{-1} \delta \hat{\mathbf{u}}_{\text{vac}}[\Omega] \quad (\text{II.74})$$

On resonance ($\Delta = 0$), the \mathbf{M}_Δ matrix becomes diagonal, allowing us to write

$$\begin{pmatrix} \delta\hat{p}_{\text{ref}}[\Omega] \\ \delta\hat{q}_{\text{ref}}[\Omega] \end{pmatrix} = \left(\kappa_1 \frac{\kappa/2 + i\Omega}{(\kappa/2)^2 + \Omega^2} - 1 \right) \begin{pmatrix} \delta\hat{p}_{\text{in}}[\Omega] \\ \delta\hat{q}_{\text{in}}[\Omega] \end{pmatrix} + \sqrt{\kappa_1\kappa_2} \frac{\kappa/2 + i\Omega}{(\kappa/2)^2 + \Omega^2} \begin{pmatrix} \delta\hat{p}_{\text{vac}}[\Omega] \\ \delta\hat{q}_{\text{vac}}[\Omega] \end{pmatrix} \quad (\text{II.75})$$

$$\delta\hat{\mathbf{u}}[\Omega] = \frac{\sqrt{\kappa_1}}{\kappa/2 - i\Omega} \delta\hat{\mathbf{u}}_{\text{in}}[\Omega] + \frac{\sqrt{\kappa_2}}{\kappa/2 - i\Omega} \delta\hat{\mathbf{u}}_{\text{vac}}[\Omega] \quad (\text{II.76})$$

such that constructing our amplitude-phase two-photon quadratures yields

$$\Gamma\delta\hat{\mathbf{u}}[\Omega] = \begin{pmatrix} \delta\hat{p}[\Omega] \\ \delta\hat{q}[\Omega] \end{pmatrix} = \frac{\sqrt{\kappa_1}}{\kappa/2 - i\Omega} \begin{pmatrix} \delta\hat{p}_{\text{in}}[\Omega] \\ \delta\hat{q}_{\text{in}}[\Omega] \end{pmatrix} + \frac{\sqrt{\kappa_2}}{\kappa/2 - i\Omega} \begin{pmatrix} \delta\hat{p}_{\text{vac}}[\Omega] \\ \delta\hat{q}_{\text{vac}}[\Omega] \end{pmatrix} \quad (\text{II.77})$$

$$\begin{aligned} \delta\hat{p}[\Omega] &= \frac{\sqrt{\kappa_1}}{\kappa/2 - i(\Delta + \Omega)} \delta\hat{p}_{\text{in}}[\Omega] + \frac{\sqrt{\kappa_2}}{\kappa/2 - i(\Delta + \Omega)} \delta\hat{p}_{\text{vac}}[\Omega] \\ \delta\hat{q}[\Omega] &= \frac{\sqrt{\kappa_1}}{\kappa/2 + (\Delta + \Omega)} \delta\hat{q}_{\text{in}}[\Omega] + \frac{\sqrt{\kappa_2}}{\kappa/2 + i(\Delta + \Omega)} \delta\hat{q}_{\text{vac}}[\Omega]. \end{aligned} \quad (\text{II.78})$$

$$\hat{\mathbf{u}}[\Omega] = \sqrt{\kappa_1} \begin{pmatrix} \chi_c[\Omega] \\ \chi_c^*[-\Omega] \end{pmatrix} \hat{\mathbf{u}}_{\text{in}}[\Omega] + \sqrt{\kappa_2} \begin{pmatrix} \chi_c[\Omega] \\ \chi_c^*[-\Omega] \end{pmatrix} \hat{\mathbf{u}}_{\text{vac}}[\Omega] \quad (\text{II.79})$$

and the intracavity quadratures as

Setting $\Delta = 0$, we can now construct the amplitude-phase two-photon quadratures as in the previous subsection which give us we now focus on

$$\begin{aligned} \delta\hat{p}[\Omega] &= \frac{\sqrt{\kappa_1}}{\kappa/2 - i\Omega} \delta\hat{p}_{\text{in}}[\Omega] + \frac{\sqrt{\kappa_2}}{\kappa/2 - i\Omega} \delta\hat{p}_{\text{vac}}[\Omega] \\ \delta\hat{q}[\Omega] &= \frac{\sqrt{\kappa_1}}{\kappa/2 - i\Omega} \delta\hat{q}_{\text{in}}[\Omega] + \frac{\sqrt{\kappa_2}}{\kappa/2 - i\Omega} \delta\hat{q}_{\text{vac}}[\Omega] \end{aligned} \quad (\text{II.80})$$

II.3 Numerical Methods and Simulations

Chapter III

Theory: Frequency Dependent Squeezing & Membrane based Optomechanics

This chapter will cover the elementary concepts required to describe an membrane based optomechanical system in a quantum regime. We will first recall basics on optical field quantization as well describing coherent and squeezed light field, to then turn to the more specific frequency dependent squeezed light field. Secondly, we will cover the mathematical description of a mechanical resonator interacting with a generic coherent optical field, highlighting the differences with the seminal optomechanical system of a mirror on a spring. Finally, we will derive the equations of motions of a membrane based optomechanical system with frequency dependent squeezed optical fields.

Contents

III.1 Frequency Dependent Squeezing	24
III.2 Cavity Optomechanics with Membrane based systems	24
III.2.1 Radiation Pressure Coupling	24
III.2.2 Quantum Langevin Equations	24
III.2.3 Mechanical Resonators	24
III.2.4 Noise spectra	24

III.1 Frequency Dependent Squeezing

III.2 Cavity Optomechanics with Membrane based systems

III.2.1 Radiation Pressure Coupling

III.2.2 Quantum Langevin Equations

III.2.3 Mechanical Resonators

Mechanical Resonators

III.2.4 Noise spectra

We will derive the Hamiltonian formalism of a three mirror cavity, and show how it can be used to describe the optomechanical coupling of a membrane in the cavity. We now have to consider two optical modes coupled to one another through the membrane transmittivities. The Hamiltonian of the system can be written as:

$$\hat{H} = \hbar\omega_1\hat{a}_1^\dagger\hat{a}_1 + \hbar\omega_2\hat{a}_2^\dagger\hat{a}_2 + \hbar g(\hat{a}_1^\dagger\hat{a}_2 + \hat{a}_2^\dagger\hat{a}_1) + \frac{\hat{p}^2}{2m} + \frac{1}{2}m\omega_m^2\hat{x}^2 \quad (\text{III.1})$$

where \hat{a}_1 and \hat{a}_2 are the annihilation operators of the two optical modes, ω_1 and ω_2 their respective frequencies, g the optomechanical coupling strength, \hat{p} and \hat{x} the momentum and position operators of the membrane, m its mass and ω_m its mechanical frequency. The optomechanical coupling strength g is defined as:

$$g = \frac{\omega_1}{L} \sqrt{\frac{\hbar}{2m\omega_m}} (T_1 + T_2) \quad (\text{III.2})$$

where T_1 and T_2 are the transmittivities of the two optical modes through the membrane. The Hamiltonian can be diagonalized by introducing the normal modes of the system, which are the eigenstates of the Hamiltonian. The normal modes can be expressed as:

$$\hat{b}_1 = \frac{1}{\sqrt{2}} (\hat{a}_1 + \hat{a}_2), \quad \hat{b}_2 = \frac{1}{\sqrt{2}} (\hat{a}_1 - \hat{a}_2) \quad (\text{III.3})$$

The normal modes \hat{b}_1 and \hat{b}_2 are the symmetric and antisymmetric modes of the system, respectively. The Hamiltonian can then be rewritten in terms of the normal modes as:

$$\hat{H} = \hbar\omega_1\hat{b}_1^\dagger\hat{b}_1 + \hbar\omega_2\hat{b}_2^\dagger\hat{b}_2 + \hbar g(\hat{b}_1^\dagger\hat{b}_2 + \hat{b}_2^\dagger\hat{b}_1) + \frac{\hat{p}^2}{2m} + \frac{1}{2}m\omega_m^2\hat{x}^2 \quad (\text{III.4})$$

Diagonalisation of two non-degenerate, tunnel-coupled optical cavities. Let a_1 and a_2 (with the usual bosonic commutation relations) annihilate photons in the first and

second cavity, whose bare resonance frequencies are $\omega_1 \neq \omega_2$. Photon tunnelling at rate $J > 0$ through the semi-transparent middle mirror couples the two modes, giving the second-quantised Hamiltonian

$$H = \hbar \begin{pmatrix} a_1^\dagger & a_2^\dagger \end{pmatrix} \underbrace{\begin{pmatrix} \omega_1 & J \\ J & \omega_2 \end{pmatrix}}_{\mathbf{M}} \begin{pmatrix} a_1 \\ a_2 \end{pmatrix}.$$

Diagonalising the 2×2 Hermitian matrix \mathbf{M} one finds the normal-mode (super-mode) eigenfrequencies

$$\omega_\pm = \frac{\omega_1 + \omega_2}{2} \pm \sqrt{J^2 + \left(\frac{\omega_1 - \omega_2}{2}\right)^2}, \quad (\text{III.5})$$

and introduces a mixing angle θ via

$$\tan 2\theta = \frac{2J}{\omega_2 - \omega_1}, \quad 0 < \theta < \pi/2.$$

The corresponding canonical operators

$$A_+ = \cos \theta a_1 + \sin \theta a_2, \quad A_- = -\sin \theta a_1 + \cos \theta a_2,$$

obey $[A_\mu, A_\nu^\dagger] = \delta_{\mu\nu}$ and bring the Hamiltonian to the diagonal form

$$H = \hbar \omega_+ A_+^\dagger A_+ + \hbar \omega_- A_-^\dagger A_-,$$

revealing two independent harmonic oscillators whose frequency splitting $\omega_+ - \omega_- = 2\sqrt{J^2 + [(\omega_1 - \omega_2)/2]^2}$ interpolates smoothly between the strong-coupling limit ($\omega_1 \approx \omega_2$) and the large-detuning regime where each cavity mode retains its individuality and the admixture of its neighbour is suppressed by the small parameter $J/|\omega_2 - \omega_1| \ll 1$.

Chapter IV

Experimental Methods

This chapter will cover the experimental methods used in the development of optomechanical systems, focusing on the generation of squeezed light and the techniques for optical locking and quadrature measurement. The methods are designed to enhance the sensitivity of measurements in quantum optics and optomechanics.

Contents

IV.1 Optical Locking Techniques with PyRPL	28
IV.1.1 Proportion-Integral (PI) Controllers	28
IV.1.2 Temperature Locks	30
IV.1.3 Optical paths Locks - Dither Locks	30
IV.1.4 Side of Fringe Locks	31
IV.1.5 Pound-Drever-Hall Locks	31
IV.1.6 Offset frequency Locks	32
IV.1.7 Coherent Sideband Locks	32
IV.1.8 PyRPL Control Implementation	32
IV.2 Optical Cavities and Squeezed Light Generation	32
IV.2.1 Cavity Types and Alignement Procedures	33
IV.2.2 Bowtie-type Optical Parametric Oscillator (OPO)	33
IV.2.3 Phase Matching and Nonlinear Crystals	33
IV.2.4 Filter Cavities for Squeezing Rotation	33
IV.3 Quadrature Measurement Techniques	33
IV.3.1 Direct Detection with Photodiodes	33
IV.3.2 Balanced Homodyne Detection	33
IV.3.3 Local Oscillator Design and Control	33

IV.1 Optical Locking Techniques with PyRPL

A central aspect of the experimental setups is the ability to stabilize various optical features. In this work, it is the case for the relative phase between two optical paths, keeping optical cavities on resonance, or fixing the detuning between a master and a slave laser.

This section will cover the locking techniques used in this work, from basic Michelson-type locking to more advanced Pound-Drever-Hall techniques and phase-locked loops. The implementation of these techniques using the in-house library PyRPL is presented.

IV.1.1 Proportion-Integral (PI) Controllers

Proportional-Integral (PI) controllers are widely used in quantum optics experiments to stabilize critical parameters such as cavity length, laser frequency, and optical phase. To this end, one needs to extract an error signal $\epsilon(t)$ that quantifies the deviation from a desired setpoint, such as a target temperature, phase difference or cavity resonance. It is typically expressed as the difference between a measured signal and its reference value:

$$\epsilon(t) = s_{\text{meas}}(t) - s_{\text{ref}},$$

where $s_{\text{meas}}(t)$ denotes the physical quantity monitored in the experiment (e.g., reflected intensity or interferometric signal), and s_{ref} is the target value corresponding to the lock point.

For effective feedback stabilization, the error signal must satisfy several essential criteria:

- **High SNR:** Near the setpoint, $\epsilon(t)$ should exhibit a high SNR to ensure robust locking and minimize the influence of technical and electronic noise.
- **Linearity and antisymmetry:** The error signal should be linear and antisymmetric in a neighborhood of the operating point. Small deviations from the setpoint should produce a proportional response in $\epsilon(t)$, with opposite signs for deviations of opposite direction.
- **Monotonicity and uniqueness:** The slope $\partial\epsilon/\partial x$, where x denotes the control parameter (e.g., cavity length or laser frequency), should be monotonic and unambiguous near the lock point to avoid multiple equilibrium points and ensure stable locking behavior.
- **Steep slope near the setpoint:** A steeper slope improves sensitivity to small deviations and enhances lock accuracy, although it must be balanced against potential noise amplification.

- **Bandwidth compatibility:** The spectral content of $\epsilon(t)$ must be compatible with the bandwidth of the actuator and the dynamics of the system. For example, in the case of a piezoelectric transducer, which acts as a low-pass mechanical element, the error signal high-frequency components won't be compensated by the actuator.

The PI controller computes the feedback signal $u(t)$ from the error signal $\epsilon(t)$ according to:

$$u(t) = K_P \epsilon(t) + K_I \int_0^t \epsilon(\tau) d\tau \quad (\text{III.1})$$

where K_P and K_I are the proportional and integral gains, respectively. The proportional term $K_P \epsilon(t)$ responds to the current error and primarily acts on mid-frequency deviations, enabling rapid corrections. The integral term $K_I \int \epsilon(\tau) d\tau$ accumulates past errors and is most effective at low frequencies, helping to eliminate long-term drifts and steady-state offsets.

In classical control theory, PID (Proportional-Integral-Derivative) controllers are designed to stabilize dynamic systems by combining three terms: a proportional term for immediate response, an integral term to eliminate steady-state error, and a derivative term that anticipates future error based on the rate of change. However, in practical experimental setups—particularly in quantum optics—PI control (Proportional-Integral) is typically sufficient and even preferable to full PID control. The derivative term, which acts predominantly at high frequencies, is generally unnecessary and can be counterproductive. This is because the feedback actuator is often a piezoelectric transducer, which exhibits non-zero capacitance. Combined with the finite output impedance of the control electronics, this forms a natural low-pass filter that significantly attenuates high-frequency components of the feedback signal. As a result, any derivative term—which primarily targets high-frequency correction—would be both ineffective due to this filtering and potentially harmful by injecting high-frequency noise into the loop.

Therefore, PI control offers a balanced and robust approach: the integral term suppresses low-frequency drifts (typically below a few Hz to tens of Hz), the proportional term corrects intermediate-frequency deviations (up to a few kHz), and high-frequency components (above the mechanical resonance or actuation bandwidth) are naturally filtered out and deliberately left uncorrected. This allows for stable feedback while preserving high-frequency signals—such as thermal noise or mechanical sidebands—which carry essential physical information for analysis and measurement.

IV.1.2 Temperature Locks

A first example of a PI lock used in this work is the temperature lock, which is used to stabilize the temperature of non linear crystals embedded inside optical cavities. The error signal is derived from a temperature sensor, such as a thermistor, which measures the temperature of the crystal and simply written as:

$$\epsilon(\Delta T) \propto \Delta T \quad (\text{IV.1})$$

where $\Delta T = T_{\text{meas}} - T_{\text{set}}$. The error signal is then fed into a PI controller, which adjusts the heating element, a peltier module in our case, to maintain the desired temperature setpoint.

The temperature lock is crucial for maintaining the phase matching conditions in nonlinear optical processes (developped in the next section), such as second-harmonic generation or optical parametric oscillation, where the efficiency of frequency conversion depends sensitively on the crystal temperature. By stabilizing the temperature, we ensure that the nonlinear interactions remain optimal, leading to consistent and reproducible results in experiments involving squeezed light generation or other nonlinear optical phenomena.

IV.1.3 Optical paths Locks - Dither Locks

Controlling the relative path length between two arms of an interferometer is a fundamental technique in quantum optics. The basic idea is to use the interference of light from two paths to lock the phase difference between them. Although not being the same experiental setups, Michelson interferometers, Mach-Zhender interferometers, and Local Oscillator stabilization error signals fall in the same category as they are derived from the same principle. Namely, the error signal is proportional to the sine of the phase difference between the two arms:

$$\epsilon(\Delta\phi) \propto \sin(\Delta\phi) \simeq \Delta\phi \quad (\text{IV.2})$$

where $\Delta\phi = \phi_a - \phi_b$ is the phase difference between the two optical paths. Analogically, we would need to add an adjustable voltage offset, as to be able to tune the error signal to zero at the desired phase difference, before seeding this error signal to the PI block. Digitally, this is performed by adding a constant offset to the error signal, which can be adjusted to set the desired phase difference.

In practice, this is implemented by mounting a mirror on which one of the arms is reflected, and then using a piezoelectric transducer to control the position of the mirror, hence modulating the relative phase between the two optical paths. The piezo is then feedback controlled

through a PI loop, which adjusts the voltage applied to the piezo to set the error signal to 0.

FIGURE

IV.1.4 Side of Fringe Locks

$$\epsilon(\Delta\omega) \propto \Delta\omega \quad (\text{IV.3})$$

IV.1.5 Pound-Drever-Hall Locks

Another key technique extensively used in this work is the *Pound-Drever-Hall* (PDH) method, a high-sensitivity scheme for stabilizing either the cavity length to a fluctuating laser frequency, or vice versa. The method relies on imposing phase modulation sidebands on the laser field, typically using an electro-optic modulator (EOM), and using these sidebands as phase-stable references. Because they lie far outside the cavity linewidth ($\Omega_{\text{mod}} \gg \kappa$), the sidebands are reflected nearly unchanged: $r(\omega_\ell \pm \Omega_{\text{mod}}) \approx 1$. In contrast, the carrier field near resonance acquires a frequency-dependent phase shift upon reflection, captured by the complex cavity reflection coefficient $r_c(\delta)$. The PDH error signal is obtained by detecting the reflected beam and demodulating the photocurrent at the modulation frequency, isolating the beat terms between carrier and sidebands. The resulting signal is proportional to the *imaginary part* of $r_c(\delta)$, which varies antisymmetrically with detuning and provides a zero-crossing error signal ideal for linear feedback. The error signal near resonance is then given by

$$\epsilon(\Delta\omega) \propto \Im(r_c(\Delta\omega)) \simeq \Delta\omega \quad (\text{IV.4})$$

This imaginary component encodes the rapid phase dispersion near resonance that allows the system to discriminate the sign and magnitude of frequency deviations. In contrast, the real part of $r_c(\delta)$, being symmetric around resonance, does not yield a usable error signal.

The *demodulation phase* plays a critical role in selecting the appropriate quadrature of the signal for feedback. Since the beat signal between the carrier and sidebands has both in-phase (cosine) and quadrature (sine) components, choosing the correct demodulation phase ensures that the extracted error signal aligns with the imaginary part of the reflection coefficient. A misaligned demodulation phase can lead to mixing of the symmetric (real) part into the error signal, thereby reducing sensitivity and introducing offset or distortion near the lock point. In practice, the demodulation phase is optimized empirically—either via a variable phase shifter in the electronic demodulation path or by adjusting the physical delay in the reference oscillator—to maximize the slope of the error signal at zero-crossing, corresponding to pure detection of the dispersive component.

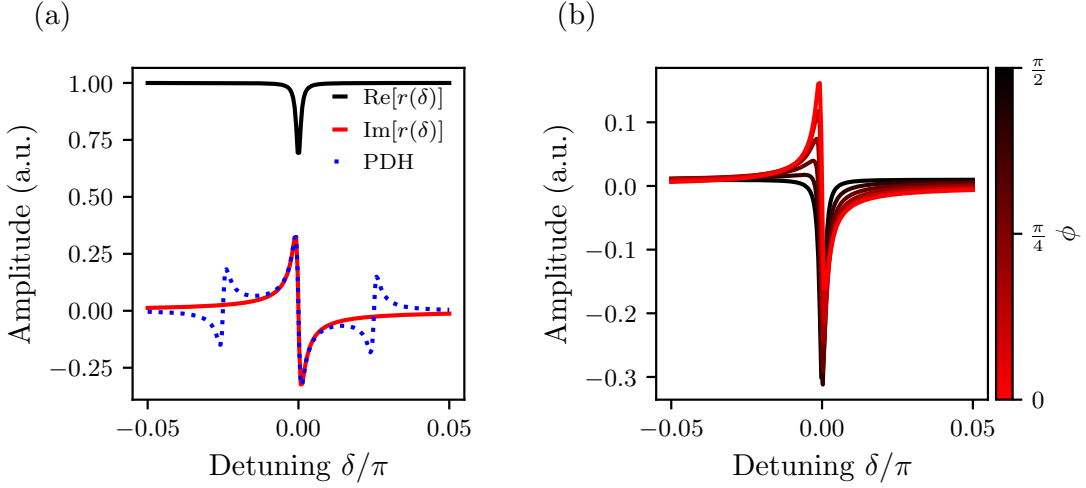


Fig. IV.1 *Schematic of the Pound-Drever-Hall (PDH) locking technique.* The laser passes through an electro-optic modulator (EOM) generating phase modulation sidebands. The modulated beam is incident on the optical cavity, and the reflected light is detected by a photodiode (PD). The photocurrent is demodulated at the modulation frequency to produce the PDH error signal, which is fed to a PI controller driving the cavity actuator (e.g., piezo). Key components are labeled: EOM (electro-optic modulator), PD (photodiode), LO (local oscillator for demodulation), and PI (proportional-integral controller).

IV.1.6 Offset frequency Locks

$$\epsilon(\Delta\omega_{\text{beat}}) \propto \Delta\omega_{\text{beat}} \quad (\text{IV.5})$$

IV.1.7 Coherent Sideband Locks

IV.1.8 PyRPL Control Implementation

IV.2 Optical Cavities and Squeezed Light Generation

Maybe I need to add a section on the theory of squeezed light generation, but for now I will just focus on the experimental methods.

IV.2.1 Cavity Types and Alignment Procedures**IV.2.2 Bowtie-type Optical Parametric Oscillator (OPO)****IV.2.3 Phase Matching and Nonlinear Crystals****IV.2.4 Filter Cavities for Squeezing Rotation****IV.3 Quadrature Measurement Techniques****IV.3.1 Direct Detection with Photodiodes****IV.3.2 Balanced Homodyne Detection****IV.3.3 Local Oscillator Design and Control**

Chapter V

Experiments: Optomechanics

This chapter will cover the experimental methods used in the development of optomechanical three-mirror cavity systems, focusing on the design, fabrication, and characterization of mechanical resonators within optical cavities. The methods are designed to enhance the sensitivity of measurements in quantum optics and optomechanics.

Contents

V.1 System Description and Setup	36
V.1.1 Previous LKB work and Motivation	36
V.1.2 Specifications and Design	37
V.1.3 Flexure Actuation	42
V.1.4 Experimental Setup	43
V.1.5 Alignment Procedures	45
V.2 Experimental Characterization	47
V.2.1 Cavity Scans and Resonance Fitting	47
V.2.2 Locking Techniques and Stability	47
V.2.3 Optical Ringdowns and Loss Measurements	47
V.2.4 Mechanical Resonator Characterization	47
V.2.5 Bistability	47
V.3 Design of an Optomechanical Fibered Cavity	47
V.3.1 Design considerations	47

Over the past two decades, optomechanical systems have greatly benefited from advancements in optical coating technologies, enabling the realization of high-finesse cavities ($\mathcal{F} > 10^5$)[?]. Simultaneously, progresses in micro/nanofabrication allowed the making of mechanical structures with high Q factors ($> 10^6$)[?]. Despite these achievements, a significant challenge remained: fabricating mechanical elements that possess both high Q and high reflectivity, as optical, mechanical and thermal effects often degrade system performance and hinder ultra-sensitive measurements[?].

V.1 System Description and Setup

V.1.1 Previous LKB work and Motivation

Previous optomechanics experiments at LKB have primarily utilized Fabry–Pérot cavities with two mirrors, where the end mirror of the cavity was typically a HR mirror deposited on top of a mechanical structure featuring a mechanical mode of interest [?].

- Over Aurélien’s and Leonard’s PhD works, the group in collaboration with ONERA developed a platform based on a 1-mm-thick quartz micropillar with an effective mass of $33 \mu\text{g}$. The structure supports a fundamental compression mode oscillating at 3.6 MHz, with a mode shape as shown in Fig. ???. Using a dry-film photoresist technique, a $100 \mu\text{m}$ diameter high-reflectivity mirror was deposited on one end of the pillar. Careful design of the suspension has yielded mechanical quality factors up to 3×10^6 at room temperature and up to 7×10^7 below 1 K. When integrated into a $50 \mu\text{m}$ -long Fabry–Pérot cavity with a custom-fabricated coupling mirror, finesses exceeding 10^5 were achieved. Importantly, this compact cavity remains robust against vibrations of the dilution refrigerator and maintains alignment during cooldown, thereby providing a stable platform to study optomechanical effects in the intermediate mass regime.
limitations and why it didnt work
- Then over Rémi’s and Michael’s PhD, another resonator was developed in collaboration with Francesco Marin’s team, based on a suspended silicon disk. The device operates in a balanced mode, where the central disk vibrates in opposition to four surrounding counterweights. By adjusting the geometry, the resonance frequency was increased to 280 kHz, corresponding to an effective mass of about $110 \mu\text{g}$, bringing the system closer to the micropillar parameters. A HR mirror was then deposited on top using the same technique as the micropillar. Finesse of about ~ 50000 were then reached. At cryogenic temperature, optimized designs reached mechanical quality factors on the order of 1.2×10^6 .**limitations and why it didnt work**

Although the systems ended up being limited by various factors mentioned above (optical, mechanical and thermal effects) [?], the parts designed over the years did feature a high level of passive stability as well as good thermalization properties. A pivotal solution, introduced by Regal, Kimble, Harris, and collaborators[?, ?], was to decouple these requirements by embedding a high- Q mechanical resonator within a high-finesse optical cavity, using the optical field to probe and control the resonator's dynamics.

V.1.2 Specifications and Design

It was then decided to build on this design and extend it to a three-mirror cavity in a Membrane-At-The-Edge configuration (MATE) to benefit from this large linear coupling range as detailed in the previous chapter. That is the work Michael and myself undertook during my M2 internship and the first year of my PhD. This new three mirror cavity then needed to fulfill various requirements:

- **High Finesse:** input and back mirrors should both have high reflectivities, with low extra losses such as scattering, absorption, etc ...[?]
- **High Q factor:** the middle mirror i.e. the mechanical resonator, should feature a high Q factor, ideally above 10^6 , in order to ensure a good sensitivity to radiation pressure forces[?]
- **Optical alignment:** the cavity should be designed to allow for easy optical alignment, with the ability to mode match the setup fairly easily.
- **Dynamical range:** both input and output mirrors should be mounted on piezoelectric actuators, allowing for a dynamic range of at least few microns to scan few FSRs. The piezo actuators should also be able to provide a good bandwidth, ideally above 100 kHz, as well as a sub-nanometer resolution to ensure a good control of the cavity length[?].
- **Compactness & Stability :** the entire assembly should be compact, with a high level of passive stability, yet without mechanically low pass filtering the piezo actuators motion during the locking.
- **Vacuum and Cryogenic compatibility:** the cavity should be vacuum compatible, and the mirrors should be thermally anchored to the vacuum chamber in order to ensure a good thermalization of the system. Same holds for the cryogenic compatibility, although no test could be performed during this thesis. The cavity was nonetheless designed to be compatible with cryogenic operation.

High Finesse

Low loss mirrors were produced by **Jérôme DEGALLAIX** and **David HOFMAN** at the *Laboratoire des Matériaux Avancés* (LMA, Lyon) using ion-beam-sputtered (IBS) Bragg stacks made of Ta_2O_5 (high index, $n \approx 2.09$) and SiO_2 (low index, $n \approx 1.46$)^[?, ?].

The coatings were deposited in the LMA's *Veeco SPECTOR* chambers and subsequently annealed at 500°C for 10 hours to minimise both optical (absorption) and mechanical losses, following the recipe of Amato *et al.* [?]. ¹

We supplied the LMA with a batch of substrates with various radii of curvature to explore different cavity geometries:

- **Plane substrates:** Laseroptik S-00798
- **Plano-concave substrates:**
 - Laseroptik S-00128 ($R = 20$ mm)
 - Laseroptik S-00127 ($R = 15$ mm)
 - Laseroptik S-00126 ($R = 10$ mm)

All optics feature

- **Back-side AR:** $R \lesssim 100$ ppm. This is not critical for the cavity performance since the back side is not actually contributing to the finesse, but it is important to avoid parasitic reflections in the setup.

- **Front-side HR:**

$T \sim 20 \pm 4$ ppm on the plane mirrors,

$T \sim 50 \pm 10$ ppm and 100 ± 10 ppm on the concave mirrors, respectively,

- total round-trip scatter + absorption $\lesssim 20$ ppm, in agreement with the measurements reported (absorption ~ 0.7 ppm, scattering ~ 10 ppm) in Ref. [?].

The quarter-wave design is centred at $\lambda = 1064$ nm for normal incidence. After annealing, the measured mechanical loss angle of the $\text{TiO}_2:\text{Ta}_2\text{O}_5/\text{SiO}_2$ stack is $\phi < 4 \times 10^{-4}$ at 1 kHz [link to mechanical damping needed](#), supporting cavity finesse in the range $200\,000 - 500\,000$ before excess scatter or absorption dominates[?].

¹Identical optics are used for the Advanced LIGO, Advanced Virgo and KAGRA interferometers[?].

High Q factor

The middle mirror is a commercially–available stoichiometric silicon-nitride (Si_3N_4) membrane supplied by Norcada (NX10050AS)[?, ?]. It consists of a $0.50 \text{ mm} \times 0.50 \text{ mm}$, 50 nm -thick Si_3N_4 film suspended in a $10 \text{ mm} \times 10 \text{ mm}$, $200 \mu\text{m}$ -thick silicon frame and is marketed specifically for *high-Q* resonator applications. Because stoichiometric LPCVD Si_3N_4 is under high intrinsic tensile stress ($\sigma \approx 0.9 \text{ GPa}$), the square drum supports MHz-frequency modes with exceptionally low mechanical loss[?].

- **Room temperature.** Measurements on nominally identical Norcada membranes report quality factors $Q \sim 5 \times 10^6$ at $\approx 1 \text{ MHz}$ in $< 10^{-6} \text{ mbar}$ vacuum [?, ?].
- **Cryogenic operation.** Cooling to $T \lesssim 300 \text{ mK}$ reduces internal friction by an order of magnitude, with $Q > 10^7$ routinely observed [?].

On the basis of these results we set the following design targets:

$$Q_{\text{RT}} \geq 5 \times 10^6, \quad Q_{\text{cryogenic}} \geq 1 \times 10^7.$$

The membrane’s high stress, thin-film nature and dielectric composition make it fully compatible with ultra-high-vacuum environments and repeated cryogenic cycling, while introducing (a priori) negligible optical loss in the cavity. These attributes ensure a robust, spectrally clean mechanical resonator for advanced quantum-optomechanics experiments.

Optical alignment

The cavity is designed to be compatible with the Thorlabs cage system. The input mirror is mounted on a 3 axis cage mount, allowing for easy alignment of the input mirror with respect to the cavity optical axis. Both the resonator and the back mirror are embedded within a custom-made holder, which is itself integrated into the cage system. The relative tilt between the resonator and the back mirror is adjusted using a set of 3 screws with a very fine thread, allowing for a fine alignment of the parallelism of the back cavity. The alignment procedure is detailed in section ??.

Dynamical range

The input (front) mirror is glued to a PI P-016.00H ring-stack piezoelectric actuator using vacuum epoxy (Torr Seal). Driven from 0 to $+1000 \text{ V}$ it provides a longitudinal stroke of $5 \mu\text{m}$, a blocking force of 2.9 kN , as well as an unloaded resonance of 144 kHz , making it suitable for fast, low-noise cavity-length control.

The end-mirror–membrane assembly is mounted on a flexure holder actuated by three PD080.31 piezo chips arranged mechanically in series. Each chip yields $2 \mu\text{m}$ of travel over

a drive range of -20 to $+100\text{ V}$; the triple stack therefore supplies roughly $6\text{ }\mu\text{m}$ of coarse tuning while preserving high stiffness and sub-microsecond response.

Combining the $5\text{ }\mu\text{m}$ stroke of the front P-016.00H with the $6\text{ }\mu\text{m}$ range of the rear triple stack provides an overall cavity-length adjustment of about $11\text{ }\mu\text{m}$ — equivalent to more than 20 free spectral ranges — with sub-nanometre resolution when driven by low-noise high-voltage amplifiers.

Compactness & Stability

The entire assembly is built as a cage system using standard Thorlabs cage parts, allowing for a compact and stable assembly[?]. The cage system also allows for (relatively) easy alignment of the mirrors, as well as easy access to the piezo actuators.

Vacuum and Cryogenic compatibility

The back cavity composed of the back mirror and the middle mirror is embedded inside an Oxygen Free Copper (OFC) assembly with a circular geometry, eventually mitigating for transverse misalignment issues when going to cryogenic temperatures, the constraints compensating themselves radially with respect to the symmetry axis of the cavity assembly[?]. Furthermore, the screws used to hold the assembly together are made of brass with a thermal expansion coefficient lower than that of the OFC, tightening up the cavity when reaching cryogenic temperatures. Thorlabs cage parts are compatible with moderate vacuum operation down to $\sim 10^{-5}\text{ mbar}$ if properly degreased and ultrasound cleant, but a custom cryocompatible system to hold the input mirror would be needed for operation at cryogenic temperatures.

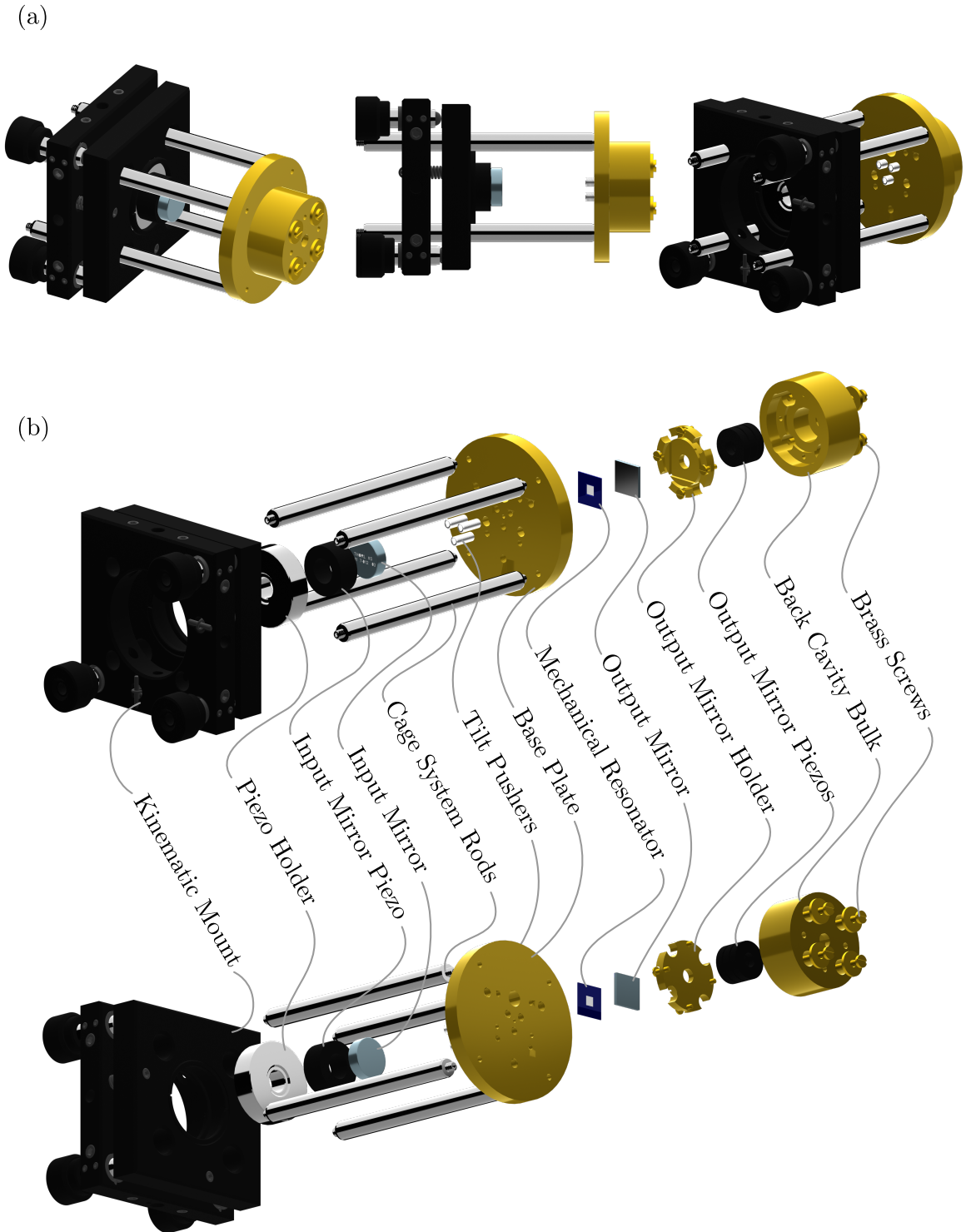


Fig. V.1 Cavity design and assembly. (a) The figure shows the overall assembly of the MATE system from various views, highlighting the integration of the high-finesse mirrors, the membrane resonator embedded inside the back cavity copper assembly held to the input mirror Thorlabs holder through a cage system.(b) The exploded view details the arrangement of the mechanical and optical components, illustrating the modular design that facilitates alignment, stability, and compatibility with vacuum environments.

The initial design of the cavity was made using Autodesk Fusion 360, allowing for a detailed 3D model of the entire assembly, including the piezo actuators, the mirrors and the cage system. The design was then exported to a STEP file format, which was used to manufacture the parts using a 3 axis CNC milling machine and a digital lathe. The pieces were machined by **Carounagarane DORE** and **Gael COUPIN** at the LKB mechanical workshop with $100\mu\text{m}$ tolerance. A detailed view of the cavity design and assembly is shown in Fig. V.1.

V.1.3 Flexure Actuation

One specificity of the MATE system is that the back cavity is significantly shorter than the front cavity, which would require high precision in both the machining of the copper pieces and the positioning of the resonator. In our case, we aim at a centimetric cavity which would require to position the membrane at roughly hundreds of microns from the back mirror, and parallel to the back mirror. Moving the membrane independently from the back mirror while maintaining a controllable tilt between both planes is therefore complicated.

A smart workaround was introduced by Jack Sankey and its group [?], where the authors introduced a flexure-tuned MATE system. The key innovation lies in actuating the membrane position by flexing its supporting silicon frame rather than translating the entire mount. This is done by mounting the back cavity in a semi-monolithic fashion, and 'locking' the silicon frame of the membrane using three screws with a fine thread, allowing for a fine adjustment of the angle of the membrane plane with respect to the back mirror plane. The piezos pushing on the back of the assembly then force the silicon frame constrained by the screws to bend, thus displacing the membrane with respect to the back mirror, as shown in Fig. V.2. This approach preserves the cavity alignment while enabling continuous and wide-range tuning of both the membrane displacement and tilt.

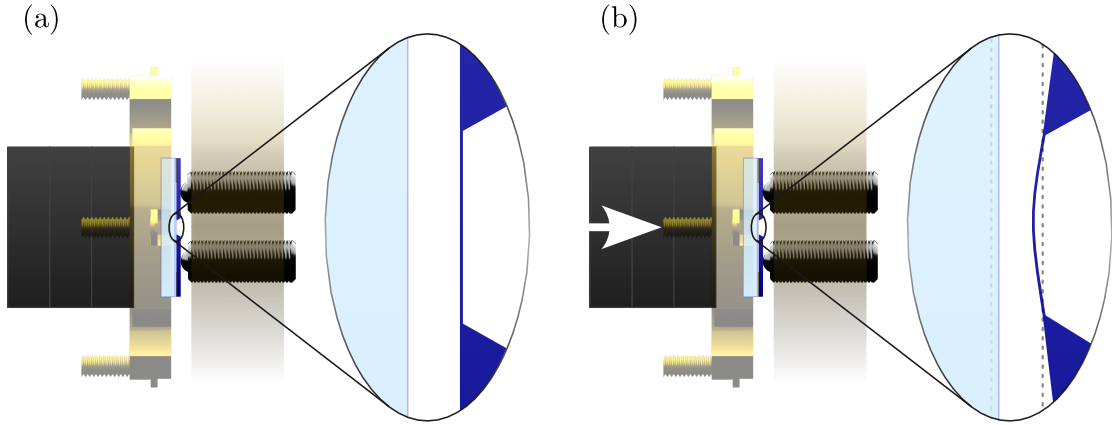


Fig. V.2 Cavity design and assembly. (a) In this configuration (no voltage applied to the piezos), the screws are used to align the membrane plane with respect to the back mirror plane, ensuring a good parallelism between both planes. (b) Flexure tuning of the membrane position. When a voltage is applied to the piezos, they push on the back of the assembly, forcing the silicon frame to bend, thus displacing the membrane with respect to the back mirror. The two dashed lines show the initial positions of the back mirror and the membrane. This push shortens the overall cavity length (i.e. increasing the overall system's frequency), as well as the relative distance between the mirror and the membrane (i.e. changing the optomechanical coupling).

V.1.4 Experimental Setup

The assembly is now to be integrated into the optical setup shown in Fig. V.3. The source laser is a 1064nm Nd:YAG laser (Coherent Mephisto). We did not require the full optical power delivered by the laser, so a short optical path not detailed here splits the laser in 3 arms to eventually fiber couple some laser power and bring it to other experiments that would need 1064nm laser light.

The optical path then consists of :

- a first half waveplate and a beam splitter to adjust the total power injected into the experimental setup,
- a fibered electro-optics phase modulator (EOM Photline NIR-MPX-LN-10) to generate sidebands for the PDH locking of the cavity. It is polarization matched by using a fibered polarization controller to avoid Residual Amplitude Modulation noise (RAM) at the output (three blue circles on the optical layout).

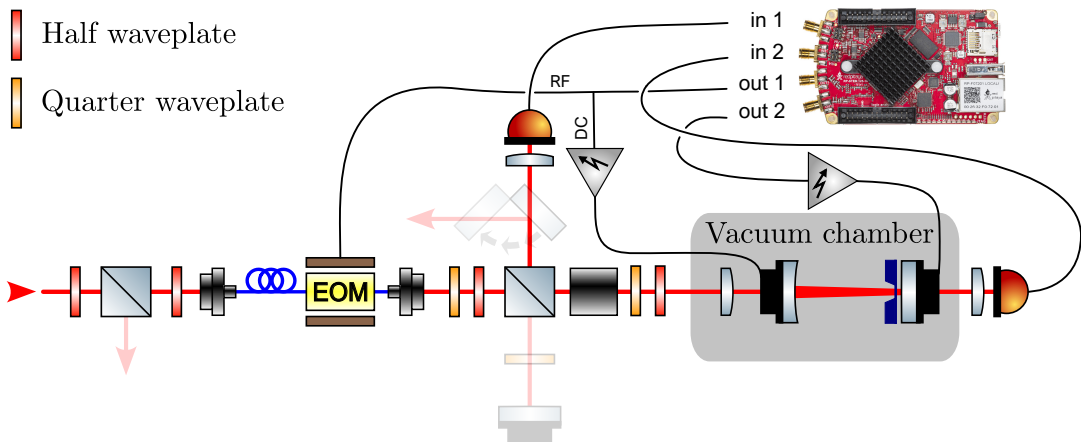


Fig. V.3

- a fiber coupler to go from a guided optical mode to a free space optical mode, with the coupler adjusted such that the outputted beam is collimated and has a waist of about 1mm,
- a quarter waveplate to compensate for ellipticity of the output beam polarization, then a half waveplate and a beam splitter to adjust the powers injected into the cavity path and the prospective LO path, respectively,
- on the cavity path, a faraday rotator to ensure the cavity reflected beam to be deflected to an output port and not back into the fiber
- a lens to mode match the laser input mode to the cavity mode, with a focal length of 40 to 60mm depending on the input mirror radii of curvature. This lens is mounted on a x-y cage system translation mount, and is mounted inside the vacuum chamber that features AR coated windows to allow for optical access yet minimal parasite reflections.
- the cavity itself.
- two photodiodes (Thorlabs ???) to detect the reflected beam and the transmitted beam, respectively, with 40mm focal length lenses to focus the beam onto the photodiodes.

The optical path was designed to be as modular as possible, allowing for easy replacement of the components if needed, as well as additions of optical elements. For this reason, it features two faint additional optical paths as seen on Fig. V.3, one for a prospective LO, and another to deflect the reflected beam to a Homodyne Detection setup using a flip mirror. Polarization optics would also need to be added on the Homodyne Detection path to mix the LO and the reflected beam, but this was not done during this thesis.

V.1.5 Alignment Procedures

The optical setup is now to be aligned as to ensure a good mode matching between the laser input mode and the cavity mode. The steps are as follows, and the associated diagrams are shown in Fig. V.4:

- **Step 1** (Fig. V.4(a)): we position an iris diaphragm before our two injection mirrors mounted on (θ_x, θ_y) kinematic mounts. We then adjust the tilt of both mirrors i.e. *beam-walking*, such that the reflected beam is centered on the iris diaphragm: this is done by maximising the reflected signal on the reflection photodiode. This ensures the beam reflected by the output mirror (HR mirror) is at normal incidence. In a second time we tune the plane of the resonator using the three screws of the assembly. We monitor the Fizeau fringes in transmission with a camera (Allied Vision Alvium), and adjust the tilt such that no fringes are to be seen.
- **Step 2** (Fig. V.4(b)): we then place the focusing lens in the optical path, and adjust its position such that we recover maximal power on the reflection photodiode. This lens is mounted on the (x-y) cage system translation mount, and positioned at a distance from the back mirror fixed by the cavity mode matching requirements (ref chap theory). The lens is then fixed in place using the cage system screws.
- **Step 3** (Fig. V.4(c)): we add the input mirror on a (θ_x, θ_y) cage system mount, and adjust its position to get an input beam normal to the tangent of the concave mirror curvature. This is also done maximising the reflected power on the reflection photodiode. The mount (and thus the mirror) was also positioned at the appropriate distance from the back mirror to ensure optimal mode matching.
- **Step 4** (Fig. V.4(d)): We scan the cavity length using the piezo actuator mounted on the input mirror, and monitor the cavity resonances using both the reflected and transmitted photodiodes. We finally fine tune the mode match by *beam-walking* the two injection mirrors. We can also play with the collimating lens at the fiber coupler (not shown on the diagram) as to fine tune for longitudinal mode matching. The cavity is now aligned and ready for operation.

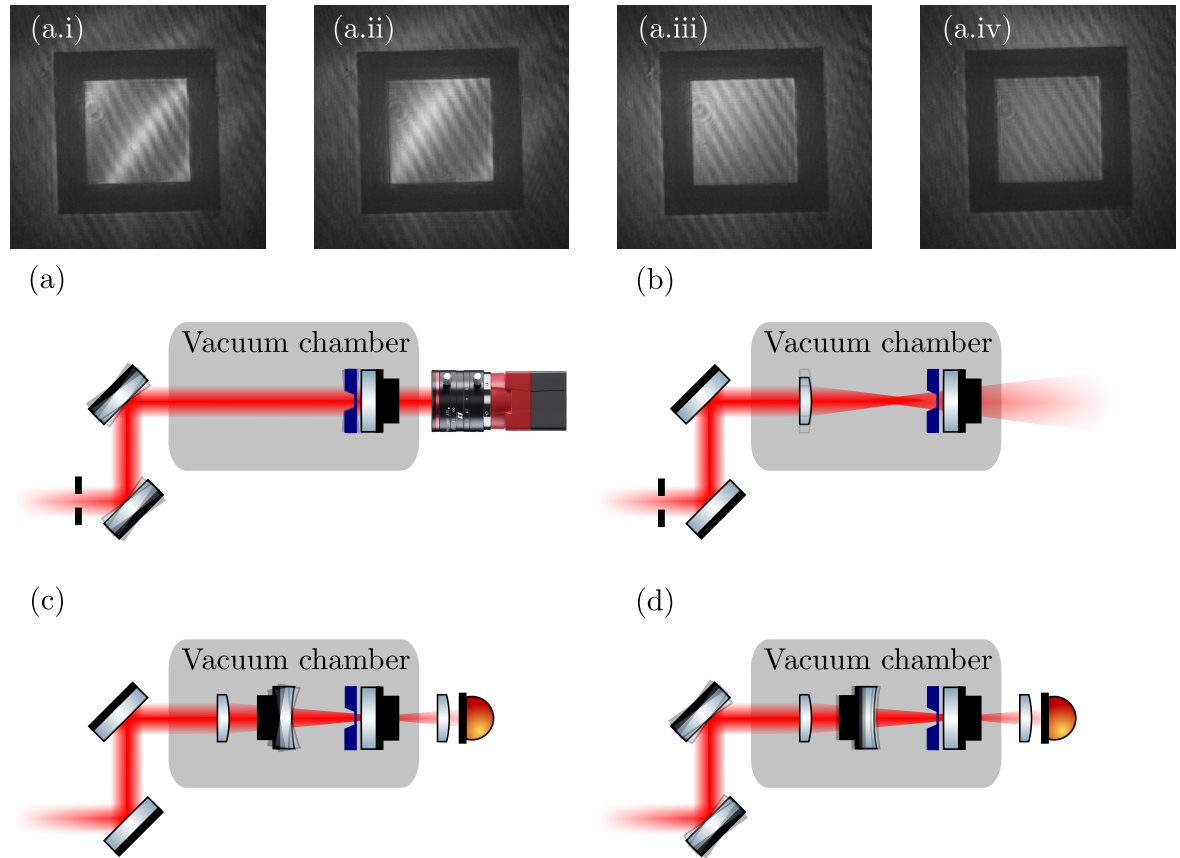


Fig. V.4 Set up alignment procedure. (a) to (d) show the steps to align the cavity with respect to the optical path (detailed in the main text). The (a.i) to (a.iv) show what is seen on the camera 4 four different tilt positions where (a.iv) displays a 'good' tilt alignment: no visible fringes except for the dim fringes of the camera setup. These dim fringes are present when the beam is a normal incidence with the back mirror (use of the iris) and are believed to be interferences arising from reflections inside the camera objective as they are seen whatever the plane of focus is.

V.2 Experimental Characterization

V.2.1 Cavity Scans and Resonance Fitting

V.2.2 Locking Techniques and Stability

V.2.3 Optical Ringdowns and Loss Measurements

V.2.4 Mechanical Resonator Characterization

V.2.5 Bistability

V.3 Design of an Optomechanical Fibered Cavity

V.3.1 Design considerations

Chapter VI

Experiments: Squeezed Light

This chapter will cover the experimental methods used in the development of frequency-dependent squeezing in optomechanical systems, focusing on the generation of squeezed light, optical locking techniques, and quadrature measurement methods. The methods are designed to enhance the sensitivity of measurements in quantum optics and optomechanics.

Contents

VI.1 OPO Resonance and Locking	50
VI.1.1 Resonance Conditions and Sweeps	50
VI.1.2 Lock Acquisition and Optimization	50
VI.1.3 Stability Characterization	50
VI.2 Quadrature Spectral Analysis	50
VI.2.1 Detection of Squeezing and Anti-squeezing	50
VI.2.2 Spectral Variation with Frequency	50
VI.2.3 Optimal Quadrature Conditions	50
VI.3 Filter Cavity Concept	50
VI.3.1 Virgo Filter Cavity	50
VI.3.2 Thermal effects in bichromatic locks	50
Appendix: PDH Derivation	53
Appendix: Spectra Derivation	57

VI.1 OPO Resonance and Locking

VI.1.1 Resonance Conditions and Sweeps

VI.1.2 Lock Acquisition and Optimization

VI.1.3 Stability Characterization

VI.2 Quadrature Spectral Analysis

VI.2.1 Detection of Squeezing and Anti-squeezing

VI.2.2 Spectral Variation with Frequency

VI.2.3 Optimal Quadrature Conditions

VI.3 Filter Cavity Concept

VI.3.1 Virgo Filter Cavity

VI.3.2 Thermal effects in bichromatic locks

Summary, conclusion and perspectives

This chapter will cover the summary of the work done, the conclusions drawn from the experiments, and the perspectives for future research in optomechanical systems. It will highlight the key findings, their implications for quantum optics, and potential directions for further exploration.

Appendix 1: Derivation of the PDH Error Signal

In this appendix, we derive the Pound-Drever-Hall (PDH) error signal starting from the real, quantum-normalized phase-modulated electric field expression. We aim to show how the demodulated signal is a linear combination of the real and imaginary parts of the cavity reflection coefficient, with the demodulation phase selecting the appropriate quadrature for locking.

1. Input Phase-Modulated Field

The electric field at the input of the cavity is assumed to be a coherent state that has been phase-modulated at frequency Ω , such that the classical (real) electric field takes the form:

$$E_{\text{cl}}^{(\text{PM})}(t) = i\sqrt{\frac{\hbar\omega_0}{2\varepsilon_0}} \alpha_0 \left[e^{-i\omega_0 t} - e^{i\omega_0 t} + \frac{i\epsilon_\phi}{2} (e^{-i(\omega_0-\Omega)t} + e^{i(\omega_0-\Omega)t}) + \frac{i\epsilon_\phi}{2} (e^{-i(\omega_0+\Omega)t} + e^{i(\omega_0+\Omega)t}) \right] \quad (1)$$

where α_0 is the coherent amplitude of the carrier, $\epsilon_\phi \ll 1$ is a small modulation index (related to the phase modulation depth), and ω_0 is the optical carrier frequency. This field includes both the positive and negative frequency components, as expected for a physical (Hermitian) electric field operator.

2. Reflection from the Cavity

Each frequency component of the field is reflected with a complex frequency-dependent amplitude reflection coefficient $r(\omega)$, such that the reflected field is:

$$\begin{aligned} E_{\text{refl}}(t) = & i\sqrt{\frac{\hbar\omega_0}{2\varepsilon_0}} \alpha_0 \left[r(\omega_0)e^{-i\omega_0 t} - r^*(\omega_0)e^{i\omega_0 t} \right. \\ & + \frac{i\epsilon_\phi}{2} \left(r(\omega_0 - \Omega)e^{-i(\omega_0-\Omega)t} + r^*(\omega_0 - \Omega)e^{i(\omega_0-\Omega)t} \right) \\ & \left. + \frac{i\epsilon_\phi}{2} \left(r(\omega_0 + \Omega)e^{-i(\omega_0+\Omega)t} + r^*(\omega_0 + \Omega)e^{i(\omega_0+\Omega)t} \right) \right] \end{aligned} \quad (2)$$

3. Photodetected Intensity

The photodetector measures the intensity:

$$I(t) \propto |E_{\text{ref}}(t)|^2$$

We isolate the terms oscillating at Ω , which arise from the interference between the carrier and sideband components. Keeping only the beat terms between the carrier and sidebands, we find:

$$I(t) \supset \epsilon_\phi \cdot \text{Re}[A_+ - A_-] \cos(\Omega t) + \epsilon_\phi \cdot \text{Im}[A_+ - A_-] \sin(\Omega t) \quad (3)$$

where we define:

$$A_\pm = r(\omega_0)r^*(\omega_0 \pm \Omega)$$

4. Demodulation with Arbitrary Phase

The signal is demodulated using a local oscillator $\cos(\Omega t + \phi)$, where ϕ is the demodulation phase. Using trigonometric identities:

$$\cos(\Omega t + \phi) = \cos(\Omega t) \cos \phi - \sin(\Omega t) \sin \phi$$

we multiply Equation (3) and low-pass filter to obtain:

$$\epsilon_{\text{PDH}}(\phi) \propto \epsilon_\phi \{ \text{Re}[A_+ - A_-] \cos \phi + \text{Im}[A_+ - A_-] \sin \phi \} \quad (4)$$

5. Sidebands Far Off-Resonance Approximation

In the standard PDH regime, the modulation frequency is much greater than the cavity linewidth:

$$\Omega \gg \kappa$$

so the sidebands are far off-resonance. This means:

$$r(\omega_0 \pm \Omega) \approx 1 \Rightarrow A_\pm \approx r(\omega_0)$$

and therefore:

$$A_+ - A_- \approx 0$$

However, if we retain the asymmetry between the sidebands (e.g., due to dispersion), or keep the finite detuning contribution, we approximate:

$$A_+ - A_- \approx r(\omega_0) [r^*(\omega_0 + \Omega) - r^*(\omega_0 - \Omega)] = r(\omega_0) \Delta r^*$$

6. Final Result

Substituting into Equation (4), we obtain:

$$\epsilon_{\text{PDH}}(\phi) \propto \epsilon_\phi \{ \text{Re}[r(\omega_0)\Delta r^*] \cos \phi + \text{Im}[r(\omega_0)\Delta r^*] \sin \phi \} \quad (5)$$

In the limit where $\Delta r^* \rightarrow 1$ (normalized, symmetric sidebands), this simplifies to:

$$\boxed{\epsilon_{\text{PDH}}(\omega_0, \phi) \propto \cos \phi \cdot \text{Re}[r(\omega_0)] + \sin \phi \cdot \text{Im}[r(\omega_0)]} \quad (6)$$

7. Interpretation

Equation (6) shows that the demodulated error signal is a linear superposition of the real and imaginary parts of the complex reflection coefficient. The demodulation phase ϕ selects the detected quadrature:

- $\phi = 0$: error signal is proportional to $\text{Re}[r]$ — symmetric around resonance, not suitable for locking.
- $\phi = \pi/2$: error signal is proportional to $\text{Im}[r]$ — antisymmetric, ideal dispersive error signal.
- $\phi \neq 0, \pi/2$: mixes quadratures, possibly introducing offset or distortion.

This derivation makes explicit how the PDH method uses phase-sensitive detection to extract the component of the reflection coefficient that varies linearly with detuning, enabling precise feedback locking of the laser to the cavity resonance.

Appendix 2: Spectra derivation

$$\hat{p}[\Omega] = 2|\alpha| \left(\delta[\Omega] + \operatorname{Re}\{\varepsilon[\Omega]\} \right) + \delta\hat{p}[\Omega], \quad (7)$$

$$\hat{p}[\Omega] \hat{p}[\Omega'] = 4|\alpha|^2 \left(\delta[\Omega]S[\Omega'] + \delta[\Omega] \operatorname{Re}\{\varepsilon[\Omega']\} + \delta[\Omega'] \operatorname{Re}\{\varepsilon[\Omega]\} + \operatorname{Re}\{\varepsilon[\Omega]\} \operatorname{Re}\{\varepsilon[\Omega']\} \right) + \delta\hat{p}[\Omega] \delta\hat{p}[\Omega'], \quad (8)$$

$$\langle \dots \rangle = 4|\alpha|^2 \left(\delta(\Omega) \delta(\Omega') + \frac{\varepsilon}{2} \delta(\Omega) \delta(\Omega' - \Omega_m) + \frac{\varepsilon}{2} \delta(\Omega) \delta(\Omega' + \Omega_m) \right) \quad (9)$$

$$+ \frac{\varepsilon}{2} \delta(\Omega') \delta(\Omega - \Omega_m) + \frac{\varepsilon}{2} \delta(\Omega') \delta(\Omega + \Omega_m) \quad (10)$$

$$+ \frac{\varepsilon^2}{4} \left[\delta(\Omega - \Omega_m) \delta(\Omega' + \Omega_m) + \delta(\Omega - \Omega_m) \delta(\Omega' - \Omega_m) \right. \quad (11)$$

$$\left. + \delta(\Omega + \Omega_m) \delta(\Omega' + \Omega_m) + \delta(\Omega + \Omega_m) \delta(\Omega' - \Omega_m) \right] \Big) + \langle \delta p[\Omega] \delta p[\Omega'] \rangle. \quad (12)$$

Sujet : Progress towards cryogenic squeezed light optomechanics

Résumé : .

Mots clés : Optomecanique, Lumière comprimée, Cavité de grande Finesse, Interferométrie, Bruit thermique, Bruit de grenaille quantique, Resonateur de grand facteur de Qualité, Interféromètres pour la detection d'ondes gravitationnelles, Bruit de pression de radiation quantique

Subject : Optomechanics and squeezed light

Abstract:

Keywords : Optomechanics, Squeezing, High-Finesse cavity, Interferometry, Thermal Noise, Quantum Shot Noise, High-Q Resonator, Gravitational wave Interferometer, Quantum Radiation Pressure Noise

